Chinese Journal of Chemical Engineering 90 (2026) 214–231

Contents lists available at ScienceDirect

Chinese Journal of Chemical Engineering

journal homepage: www.elsevier.com/locate/CJChE

Full Length Article

Dual-charged, non-swelling amine/carboxyl functionalized Fe–Mn mixed oxide composite for simultaneous removal of anionic and cationic azo dyes: Experimental and DFT studies

Afsar Khan [1], Ran Hong [1], Saisai Chen [1], Tingting Liu [1], Savaş Kaya [2], Weihua Chen [3,*], Dayong Xu [1,*]

[1] School of Chemical and Environmental Engineering, Anhui Polytechnic University, Wuhu 241000, China
[2] Sivas Cumhuriyet University, Faculty of Science, Department of Chemistry, 58140, Sivas, Turkey
[3] School of Chemistry and Environmental Science, Shangrao Normal University, Shangrao 334000, China

ARTICLE INFO

Article history:
Received 12 July 2025
Received in revised form
16 September 2025
Accepted 17 September 2025
Available online 3 December 2025

Keywords:
Functionalization
Adsorption
Fixed-bed
Synthesis
DFT calculations
Composites

ABSTRACT

Iron (Fe) and manganese (Mn) mixed oxide composites are widely recognized for their excellent adsorption performance in wastewater treatment. However, their functionalization for simultaneous removal of both anionic and cationic contaminants remains underexplored. In this study, Fe–Mn mixed oxides were functionalized with poly(acrylic acid) (PAA) and chitosan to introduce carboxylic and amine groups respectively, forming a dual-functionalized composite (PAA–chitosan–FeMn). The material was evaluated for the adsorption of Congo red, reactive blue 19, and methylene blue from aqueous solutions using batch and fixed-bed reactor systems. The composite was characterized before and after adsorption using X-ray photoelectron spectroscope (XPS), atomic force microscope, scanning electron microscope, high-resolution transmission electron microscope, Fourier transform infrared spectroscope (FTIR), thermal gravimetric analyzer, and Raman spectroscopy. A marked enhancement in adsorption capacity was observed for all target dyes. Mechanistic investigations using XPS, FTIR, and density functional theory (DFT) indicated that the adsorption process was predominantly governed by electrostatic interactions and hydrogen bonding involving carbon, nitrogen, and oxygen functional groups. XPS analysis further confirmed the active role of Fe and Mn ions in dye binding. Comprehensive studies on adsorption isotherms, kinetics, and thermodynamics were conducted under optimized conditions. The composite exhibited a specific surface area of 27.4 to 68.4 $m^2 \cdot g^{-1}$ before and after dye adsorption and a point of zero charge of 6.5–6.8, facilitating effective adsorption of oppositely charged dyes at near-neutral pH. Batch adsorption experiments demonstrated maximum capacities of 95.0% to 99.7% for both dyes under optimal conditions (pH 8–10, 298 K). The PAA–chitosan–FeMn composite demonstrated high adsorption capacity, excellent stability under acidic conditions, and strong selectivity, highlighting its potential for the effective and simultaneous removal of anionic and cationic azo dyes from wastewater.

1. Introduction

The release of carcinogenic and mutagenic azo dyes such as aniline yellow, *o*-aminoazotoluene, benzidine, *o*-toluidine, methyl orange, Congo red, acid red, methylene blue, rhodamine blue, and reactive blue into drinking water from various natural and anthropogenic sources poses a serious environmental threat worldwide, particularly in countries like China [1,2] and Pakistan [3]. These pollutants have been shown to adversely affect both aquatic and terrestrial ecosystems [2,4,5]. Tauqeer Ahmad [6] reported that a total of 150 commercial samples of various types were collected from across Punjab, the most populous province of Pakistan, and were analyzed both qualitatively and quantitatively for the presence of reduction productsspecifically aromatic amines using GC-MS. The results revealed that most of the samples contained banned and highly carcinogenic azo dyes. Not only did the concentrations exceed the permissible limits, but in many cases,

* Corresponding authors.
E-mail addresses: chenweihua419818@sina.com (W. Chen), xdy826@ahpu.edu.cn (D. Xu).

https://doi.org/10.1016/j.cjche.2025.09.036

they were significantly elevated. Alarmingly, the highest detection rates were observed in major urban centers, with 88% of samples from Lahore and 80% from Faisalabad testing positive for these hazardous substances. This indicates widespread use of toxic azo dyes, particularly in Punjab's textile industry, and highlights a critical need for stringent regulatory controls and effective preventive measures to protect consumers from potential health risks.

So far, significant research has been reported on establishing different adsorbent materials, including zero valent copper [7], metal oxide-impregnated biochar [8], porous titania aerogel [9], MnO_2–polymer composite [10], organic–inorganic heterojunction [11], advanced magnetic adsorbents [12,13] have been used for the treatment of azo dyes with high sensitivity, high selectivity, and large adsorption capacity, however, each adsorbent material was found to be specific for anionic or cationic type of contaminants. Adsorbent materials that possess both functional groups for the simultaneous removal of cationic and anionic contaminants are scarcely reported. Furthermore, there is limited research employing a mechanistic approach to understand surface modifications of adsorbents and the role of ions with varying oxidation states during adsorption, particularly through advanced spectroscopic techniques such as XPS, AFM, TGA, SEM, HR-TEM, FTIR, and Raman spectroscopy before and after the adsorption process. Alterations to the adsorbent surface can reduce adsorption capacity and may lead to the formation of byproducts if the reaction halts at intermediate stages. Therefore, this study will investigate how adsorbates affect the adsorbent surface by examining surface configuration changes and potential degradation of active sites under different external conditions. These experiments aim to elucidate the binding mechanisms of contaminants and the resulting surface transformations, ultimately contributing to the rational design and development of more efficient adsorbent materials.

Poly(acrylic acid) (PAA), a water-soluble linear polymer that contains abundant carboxyl groups, has gained significant attention in environmental processes [14]. The most important feature of PAA is that the abundant carboxyl groups exhibit strong ability to combine with cationic dyes, however, the water-soluble property of linear PAA hinders its direct application to purify wastewater. Similarly, chitosan is the second most abundant natural polymer globally after cellulose, and serves as a source of amine functional group. It has got considerable attention from researchers as an adsorbent due to its non-toxicity, metal chelating capability, and biodegradability. However, chitosan powder tends to aggregate, making it unsuitable for column studies because of clogging and separation difficulties. It also exhibits poor chemical and mechanical stability, particularly in acidic environments [15]. PAA and chitosan combined with transition metals like Fe, Mn, Zn, and Cu, produces various active sites capable of adsorbing anionic and cationic azo dyes. The mixed-metal oxide combination converts chitosan into granular particles, making it more suitable for column studies [16].

Herein, we present a non-swelling, highly efficient, and acid-stable Fe-Mn mixed oxide material functionalized with amine and carboxylic groups for the simultaneous removal of anionic and cationic azo dyes under mild conditions. The carboxyl groups from PAA and the amine groups from chitosan chains were exposed as active binding sites for pollutant adsorption. Mechanistic insights into the adsorption process were obtained through X-ray photoelectron spectroscopy (XPS), Fourier-transform infrared spectroscopy (FTIR), and density functional theory (DFT) calculations, revealing the nature of interactions between the contaminants and the surface functional groups. Additionally, comprehensive adsorption studies including isotherm modeling, kinetic analysis, and thermodynamic evaluation were performed under optimized conditions to further elucidate the adsorption mechanism.

2. Materials and Method

2.1. Chemicals and reagents

All chemicals used in this study including Congo red (CR), reactive blue 19 (RB19), methylene blue (MB), polyacrylic acid, chitosan, were obtained from Sinopharm Chemical Reagent Co., Ltd, China. $KMnO_4$, $FeSO_4$, $FeCl_3$, NaOH, HCl, and $NaNO_3$ were of analytical grade ($\geq$99%) purchased from Beijing Bailingwei Technology Co., Ltd. (China) and were used without further purification. pH adjustments were made using buffer solutions, along with NaOH (0.01–0.1 $mol \cdot L^{-1}$) and HCl (0.01–0.1 $mol \cdot L^{-1}$) as required. Adsorbate solutions were prepared within a concentration range of 5–200 $mg \cdot L^{-1}$ for all adsorption experiments.

2.2. Preparation of PAA–chitosan–FeMn composite

The PAA–chitosan–FeMn composite was synthesized based on a literature procedure with specific modifications [17]. 12.5 g of $FeCl_3$ and 12.2 g of $FeSO_4$ were mixed into 200 ml of distilled water and stirred (500 $r \cdot min^{-1}$) for 30 min at normal temperature. Under vigorous stirring, 2.37 g of potassium permanganate ($KMnO_4$) and a 0.2 $mol \cdot L^{-1}$ sodium hydroxide (NaOH) solution was added simultaneously to a mixture of iron (III) chloride ($FeCl_3$) and iron (II) sulfate ($FeSO_4$) maintaining the pH of the resulting solution (solution A) within the range of 7–8. Meanwhile 10 g of chitosan powder was added in 300 ml of 0.1 $mol \cdot L^{-1}$ HCl and stirred for 4 h at room temperature until homogenous mixture was formed (solution B). A homogeneous mixture (solution C) was prepared by adding 1 g of PAA in 100 ml of water, followed by thorough stirring. Solutions B and C were added drop by drop into solution A and keep stirring up to 5 h. The precipitate was filtered, rinsed with water, and then dried in a vacuum oven at 328 K for 36 h to obtain the final particles.

2.3. Synthesis of PAA–chitosan–FeMn beads for column study

The beads were prepared by the following method. Briefly, 10 g chitosan was first dissolved in 300 ml of 0.1 $mol \cdot L^{-1}$ HCl solution and vigorously stirred for 4 h at room temperature to form homogenous mixtures. A specified quantity of powdered PAA/Fe–Mn binary oxide was subsequently put to chitosan solution, followed by thorough stirring until a uniform mixture was attained. The blending solution was dispensed dropwise into a 0.2 $mol \cdot L^{-1}$ aqueous NaOH solution using a syringe pump, with the syringe needle positioned close to the surface to facilitate the formation of spherical beads. The beads were left in the sodium hydroxide solution overnight, then thoroughly rinsed with distilled water until the filtrate reached a neutral pH. Finally, the beads were freeze-dried and stored in a desiccator for future use.

2.4. Adsorption experiments

The adsorbent material in the powder form (0.05–0.25 g) and 40 ml of adsorbate of different concentrations were taken in 100 ml of plastic bottles and put in a shaker for different time intervals (1–400 min). The pH, ranging from 3 to 11, was adjusted using sodium hydroxide (NaOH, 0.01–0.1 $mol \cdot L^{-1}$) and hydrochloric acid (HCl, 0.01–0.1 $mol \cdot L^{-1}$), while the temperature was provided between 298 and 328 K. The concentrations of CR, RB19, and MB during adsorption experiments were determined using a UV/Visible spectrophotometer (UV–Vis, 3J1-0015, Hitachi, Japan).

The maximum absorption wavelengths (λ_{max}) for each dye were used for accurate quantification: CR, 498 nm; RB19, 595 nm; and MB, 664 nm. Calibration curves were prepared by measuring the absorbance of standard dye solutions at their respective λ_{max} values. The equilibrium concentration (C_e) of the dyes was determined using a calibration curve spanning a range of 1 to 100 mg·g^{-1}.

2.5. Simultaneous removal study of anionic and cationic dyes

A multicomponent solution was prepared by mixing, of 50 mg·L^{-1} of each dye. Then, PAA–chitosan–FeMn (0.3 g) was mixed with 120 ml of the multicomponent solution, and the suspension was shaken in a thermostatic shaker at 298 K for 120 min. The mixture was further filtered with filter paper and analyzed by using a Hitachi UV/Visible spectrometer.

2.6. Column study

Dynamic flow experiments were carried out using a glass column with an internal diameter of 2 cm and a length of 50 cm. To ensure even flow distribution, each adsorbent bed was supported by layers of glass wool and glass beads. The column was filled with adsorbent material and gently vibrated to remove any air gaps. The solution was pumped upward using a peristaltic pump, with a fixed influent dye concentration of 50 mg·L^{-1}. A constant flow rate of 10 ml·min^{-1} was maintained, and effluent samples were collected at set intervals to track changes in dye concentration over time. The experiment was stopped once the effluent concentration matched the influent, and a breakthrough curve was constructed to evaluate the adsorption performance.

2.7. Regeneration study

Regeneration studies were carried out using 0.1 mol·L^{-1} HCl solution for CR dye. Initially, 0.1 g of the adsorbent was contacted with 40 ml of a 200 mg·L^{-1} dye solution and stirred for 3 h at 298 K to achieve dye loading. The adsorbent was then separated from the solution by centrifugation, and the adsorption capacity was determined. The dye-loaded material was thoroughly washed with distilled water and dried overnight at 353 K. For regeneration, the dried adsorbent was treated with 0.1 mol·L^{-1} HCl solution for 3 h. This adsorption/desorption cycle was repeated six times to evaluate reusability.

2.8. Characterization

The PAA–chitosan–FeMn composite was characterized before and after adsorption by Fourier transform infrared spectroscopy (FTIR, IS20, Thermo-Fisher Scientific, USA), Raman spectroscopy (LabRAM HR Evolution, Horiba, Japan), scanning electron microscopy (SEM, S-3400 N, Hitachi, Japan), transmission electron microscopy (TEM, Talos F200S, Thermo Scientific, USA), atomic force microscopy (AFM, Dimension Icon, Bruker, Germany), X-ray photoelectron spectroscopy (XPS, Nexsa G2X, Thermo-Scientific, USA), thermogravimetric analysis (TGA, DTG-60H, Shimadzu, Japan). The specific surface area of the composite before and after adsorption was measured using nitrogen adsorption–desorption isotherms at 77 K. The Brunauer–Emmett–Teller (BET) method was applied to calculate the surface area from the adsorption data. All measurements were performed using a surface area analyzer (Piod Kubo-X1000, Beijing Peiode, China). Prior to analysis, the samples were degassed at 393 K under vacuum for 6 h to remove adsorbed moisture and impurities.

2.9. Theoretical calculations

Density functional theory (DFT) calculations were conducted utilizing the B3LYP exchange-correlation functional [18,19] and LANL2DZ electronic basic set [20]. We utilized the graphics processor-based TeraChem software for our computations [21–24]. Geometry optimization was conducted with the efficient geomeTRIC energy minimizer [25]. The dispersion corrections D3 proposed by Grimme [26] were also contained to take into account the non-covalent interactions. Total dipole moment, Conceptual DFT based reactivity descriptors and binding energy were also calculated at the same level of theory. Conceptual density functional theory (CDFT) provides valuable insight into chemical stability and reactivity through parameters like electronegativity (χ), chemical potential (μ), hardness (η), and electrophilicity indexes (ω_1 and ω_2) [27,28].

$$\mu = -\chi = \left[\frac{\partial E}{\partial N}\right]_{\nu(r)} = -\left[\frac{I+A}{2}\right] \tag{1}$$

$$\eta = \left[\frac{\partial \mu}{\partial N}\right]_{\nu(r)} = \left[\frac{\partial^2 E}{\partial N^2}\right]_{\nu(r)} = I - A \tag{2}$$

$$\omega_1 = \chi^2 \Big/ 2\eta = \mu^2 \Big/ 2\eta = (I+A)^2 \Big/ 8(I-A) \tag{3}$$

$$\omega_2 = IA/(I-A) \tag{4}$$

In the equation, E represents the total electronic energy, and N denotes the total number of electrons in the chemical system. A and I are electron affinity and ionization energy, respectively. Here, for the approximately prediction of the studied chemical systems, we used the Koopmans Theorem (KT) giving the following simple relations based on orbital energies [29].

$$I = -E_{HOMO} \tag{5}$$

$$A = -E_{LUMO} \tag{6}$$

where, E_{HOMO} and E_{LUMO} represent the energies of highest occupied molecular orbital (HOMO) and lowest unoccupied molecular orbital (LUMO) orbital of the molecular chemical systems, respectively.

3. Results and Discussion

3.1. Characterization of PAA-chitosan-FeMn composite before and after adsorption

3.1.1. Surface area

The surface area of the (PAA–chitosan–FeMn) composite increased from 27.4 to 68.4 m^2·g^{-1} after dye adsorption. This could indicate changes in the adsorbent structure or pore formation during the adsorption process. The surface area of composite materials before adsorption (27.4 m^2·g^{-1}) were lower than those of after adsorption (68.4 m^2·g^{-1}). The difference in surface areas before and after adsorption process are due to the attachment of organic component of dye to the surface of composite material. Interestingly, the BET surface area of the composite increased from 27.4 to 68.4 m^2·g^{-1} after dye adsorption it can be attributed to the unique polymer-oxide structure. Interaction with dye molecules can induce slight rearrangement of polymer chains, expose previously inaccessible pores and increase the nitrogen-accessible surface area. SEM images (see Fig. 3) reveal enhanced surface roughness and pore exposure after adsorption, supporting this

interpretation. Therefore, the apparent surface area increase reflects a combination of structural reorganization and enhanced accessibility of active sites [30,31].

3.1.2. FTIR analysis

FTIR was employed to investigate the functional groups and interactions in the PAA–chitosan modified mixed oxides of iron and manganese. Fig. 1(a) shows the FTIR spectra of bare Fe-Mn mixed oxide, PAA–chitosan–FeMn composite, and dye loaded PAA–chitosan–FeMn composite. A broad and intense band observed around 3400 cm^{-1}, together with a bending vibration at approximately 1630 cm^{-1}, confirmed the presence of surface –OH groups and adsorbed water molecules, which are typical for hydrous transition-metal oxides. A weak band in the region of 950–850 cm^{-1} could be assigned to Fe–OH and Mn–OH bending vibrations, suggesting the coexistence of both hydroxylated sites that are potentially active for surface reactions. The fingerprint region was dominated by strong metal-oxygen lattice vibrations: a broad envelope between 650 and 450 cm^{-1} corresponded to Fe–O, Mn–O, and mixed Fe–O–Mn stretching modes in edge- and corner-sharing octahedra, confirming the formation of a mixed oxide framework. The peaks at ~1384 cm^{-1} and 1450–1400 cm^{-1}, when present, were attributed to residual nitrate and carbonate species, originating from precursor salts and atmospheric CO_2 adsorption, respectively. Characteristic absorption bands were observed to correspond to both polymeric and oxide components. Fig. 1(a) shows the FTIR spectra of PAA–chitosan–FeMn composite and dye loaded PAA–chitosan–FeMn composite. The broad band around 3200–3600 cm^{-1} is attributed to O–H and N–H stretching vibrations, indicating the presence of hydroxyl and amine groups from chitosan and PAA and peaks near 1700 and 1400 cm^{-1} correspond to the stretching vibrations of carboxylic acid (C=O) and symmetric/asymmetric COO^- groups from polyacrylic acid, respectively. A band around 1100–1150 cm^{-1} is associated with C–O stretching. The appearance of peaks in the range of 500–700 cm^{-1} confirms the presence of Fe–O and Mn–O bonds, indicating the successful incorporation of iron and manganese oxides. Shifts or changes in peak intensities suggest interactions between the polymers and metal oxides, indicating successful functionalization and coordination of functional groups with the oxide surface. The reduced intensity of OH stretching vibration (3434 cm^{-1}) after anionic dye adsorption suggests anion exchange, where hydroxyl groups are replaced. Similarly, shifts in the $-NH_2$/$-NH_3^+$ and $-COO^-$ bands, in addition to the reduction in –OH intensity, indicate that dual-charged functional sites interact electrostatically with dye groups, confirming their active role in simultaneous dye removal. Decreased C–O stretching vibration intensity indicates hydrogen bonding between dye molecules and surface OH groups. The observed FTIR shifts may be attributed to surface interactions involving functional groups of the adsorbent. While these spectral changes are suggestive of anion exchange processes, it should be noted that such shifts can also arise from hydrogen bonding or other surface interactions. Therefore, the present results cannot be taken as exclusive proof of anion exchange. Additional evidence, such as adsorption/desorption reversibility tests, ion-specific competition studies, or zeta potential measurements, would be necessary to conclusively differentiate the underlying mechanism [10].

3.1.3. TGA analysis

Thermogravimetric analysis (TGA) was performed to evaluate the thermal stability and compositional changes of the polyacrylic acid–chitosan functionalized iron–manganese mixed oxides (PAA–chitosan–FeMn) before and after dye adsorption. The TGA curve of fresh material showed three distinct mass loss regions (Fig. 1(b)). The initial mass loss below 473 K was due to the evaporation of surface-adsorbed water. The second major mass loss between 473 and 673 K corresponded to the thermal decomposition of organic components, primarily the degradation of chitosan and the carboxylic groups of polyacrylic acid. A third gradual mass loss above 673 K indicated the breakdown of more thermally stable organic residues and possible interactions with the oxide matrix. The remaining mass at 873–1073 K represented the stable inorganic residue, mainly composed of Fe–Mn oxides. After dye adsorption, the TGA profile of the spent material exhibited a slightly higher initial mass loss, which may be attributed to the retained moisture or weakly bound dye molecules. The mass loss in the 473–673 K range increased, suggesting the presence of additional organic content from the adsorbed dye. This region also showed a slight shift in decomposition temperature, indicating possible interactions between dye molecules and the polymer–oxide matrix. The final residue remained largely unchanged, confirming the thermal stability of the oxide backbone. These thermal behaviors confirm successful dye adsorption and indicate structural or compositional changes resulting from the interaction between dye molecules and the functionalized composite material [32].

3.1.4. XRD analysis

The XRD patterns of both Fe-Mn mixed oxide and the PAA–chitosan–FeMn composite (Fig. 1(c)) reveal no discernible diffraction peaks, indicating that both materials are amorphous in nature. In the case of the bare Fe–Mn oxide, the lack of any crystalline peaks across the typical measurement range suggests a highly disordered or nanostructure coordination network of Fe and Mn cations, without formation of long-range periodicity.

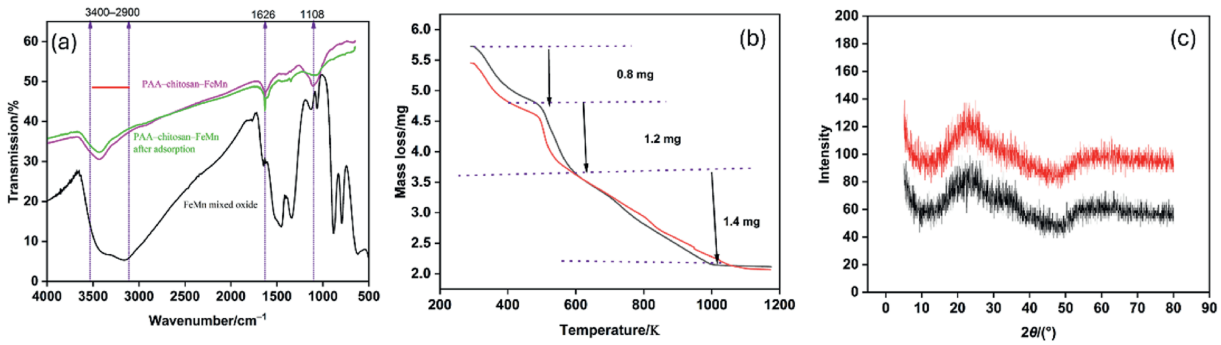

Fig. 1. (a) FTIR spectra of Fe-Mn mixed oxide and PAA–chitosan–FeMn composite before and after dye adsorption; (b) TGA plot of PAA–chitosan–FeMn composite before and after dye adsorption; (c) XRD of Fe-Mn mixed oxide and PAA–chitosan–FeMn composite.

Similarly, in the PAA–chitosan–FeMn sample, the polymeric matrix appears to hinder crystallization entirely: its presence likely suppresses nucleation and growth of ordered oxide domains, resulting in a completely amorphous composite. These observations are consistent with prior reports [33] showing that polymeric capping or embedding-especially with carboxylic-rich PAA can stabilize amorphous metal–oxide phases.

3.1.5. XPS analysis

XPS was employed to investigate the surface elemental composition, chemical states, and possible interactions in the PAA–chitosan–FeMn composite before and after dye adsorption. The survey spectrum confirmed the presence of core elements: Fe, Mn, O, C, and N, consistent with the oxide–polymer hybrid structure. The C 1s spectrum displayed peaks near 284.7 eV (C–C/C–H), 286.5 eV (C–O/C–N), and 288.5 eV (O=C–O), confirming the presence of both polyacrylic acid and chitosan. In the C 1s spectrum, peaks at 284.7 eV and 286.5 eV correspond to β-carbons and α-carbons (α-C) in the organic component, respectively (Fig. 2(a_1)). After dye adsorption, (Fig. 2(a_2)) the binding energy of α-C shifted to lower energy, and the peak intensity also decreased confirming the role of α-C in the adsorption process. The high-resolution Fe 2p spectrum showed characteristic peaks at 711.5 eV and 725 eV, corresponding to Fe $2p_3/_2$ and Fe $2p_1/_2$, indicating the presence of Fe^{2+} and the peak at 716.5 eV, corresponding Fe^{+3} (Fig. 2(b_1)). The Fe 2p spectra was based only on the general binding energy positions reported in the literature, and was therefore intended as a qualitative indication rather than a definitive assignment [34]. Similarly, Mn 2p spectra (not shown) exhibited peaks at 653.6 eV and 654 eV, corresponding to Mn $2p_3/_2$ and Mn $2p_1/_2$, consistent with Mn^{4+}/Mn^{3+} mixed oxidation states. After dye adsorption, the binding energy of Fe^{+3} was found to increase while the peak intensity decreased, indicating that complex reaction occurred between Fe and dye molecules (Fig. 2(b_2)). Moreover, Fe^{+3} has shown its role instead of Fe^{+2} in the adsorption process because the peak intensity and binding energy of Fe^{+2} was not changed. The N 1s peak at 399.4 eV was attributed to $-NH_2$ groups from chitosan (Fig. 2(c_1)). After the sorption of dye, the N 1s spectrum also showed an additional component, indicative of dye-associated nitrogen functionalities (*e.g.*, azo groups or amines). The peaks of N 1s shift to lower intensity which confirm the involvement of nitrogen in the sorption process.

The O 1s spectrum showed components associated with metal–oxygen bonds and hydroxyl/carboxyl groups. The O 1s peak shifted and broadened after sorption, implying enhanced hydrogen bonding or coordination between dye molecules and surface –OH/COOH groups. The O 1s binding energy shift from 531.4 eV to 532.4 eV after sorption suggests an increase in negative charge on oxygen atoms, likely due to changes in the electronic environment within the PAA–chitosan–FeMn composite [32]. The adsorption mechanism involves electrostatic interactions, hydrogen bonding, $\pi-\pi$ interactions, and hydrophobic interactions between the dye molecules and oxygen/nitrogen-containing functional groups on the PAA–chitosan–FeMn composite surface. The smaller change in N 1s binding energy compared to O 1s suggests nitrogen-containing groups play a key role in irreversible dye sorption on PAA–chitosan–FeMn composite. This indicates a stronger chemical affinity between the dye and nitrogen groups than oxygen groups [35].

SEM was employed to investigate the surface morphology and structural changes of PAA–chitosan–FeMn composite before and after dye adsorption. Fig. 3(a)–(e) revealed important differences in the surface morphology after dye adsorption. SEM images revealed a relatively rough and porous surface with irregularly shaped particles. The composite exhibited a loosely packed, sponge-like morphology, likely due to the integration of the biopolymer matrix (chitosan and PAA) with the metal oxide network (Fig. 3(a) and (b)). The porous architecture is favorable for adsorption, providing abundant active sites for dye interaction [17]. After dye absorption, noticeable morphological changes were observed. The surface appeared smoother and more compact, with a partial loss of porosity, suggesting that dye molecules had filled or blocked the pores. In some areas, a thin layer or film-like coverage was evident, which can be attributed to the accumulation of adsorbed dye on the surface of the composite. Additionally, agglomeration of particles was more pronounced, likely due to intermolecular interactions or bridging between dye molecules and functional groups on the adsorbent (Fig. 3(c)). This folded surface increases surface area, and this was also confirmed from surface area analysis that after dye adsorption the surface area

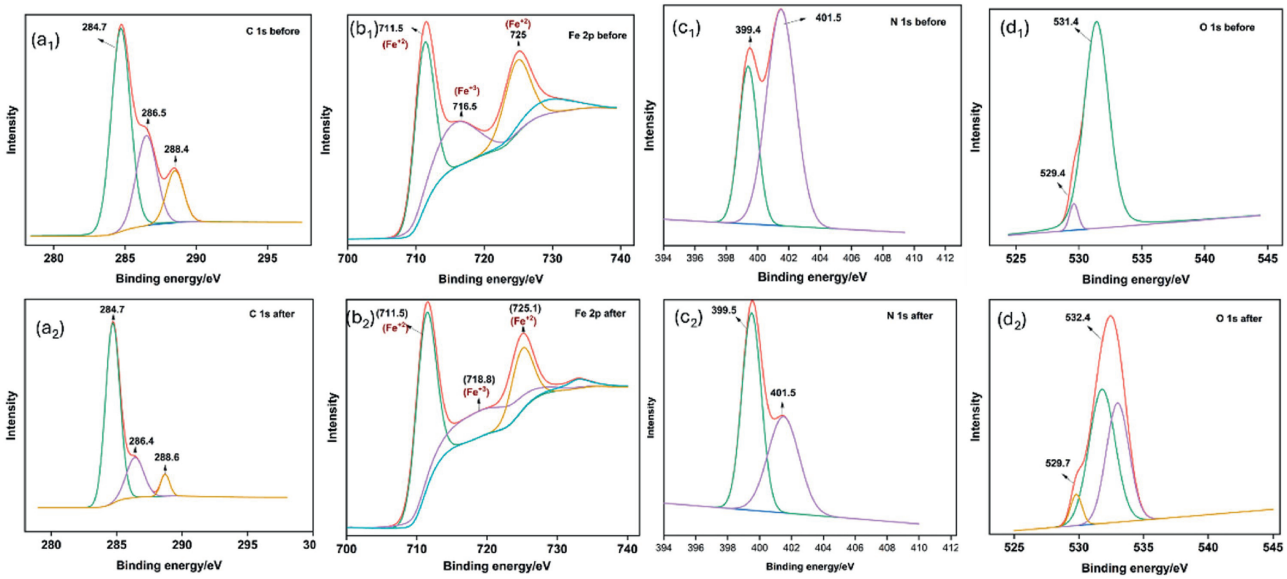

Fig. 2. XPS spectra of PAA–chitosan–FeMn composite: before dye adsorption (a_1) C 1s, (b_1) Fe 2P, (c_1) N 1s, (d_1) O 1s and after adsorption (a_2) C 1s, (b_2) Fe 2P, (c_2) N 1s, (d_2) O 1s.

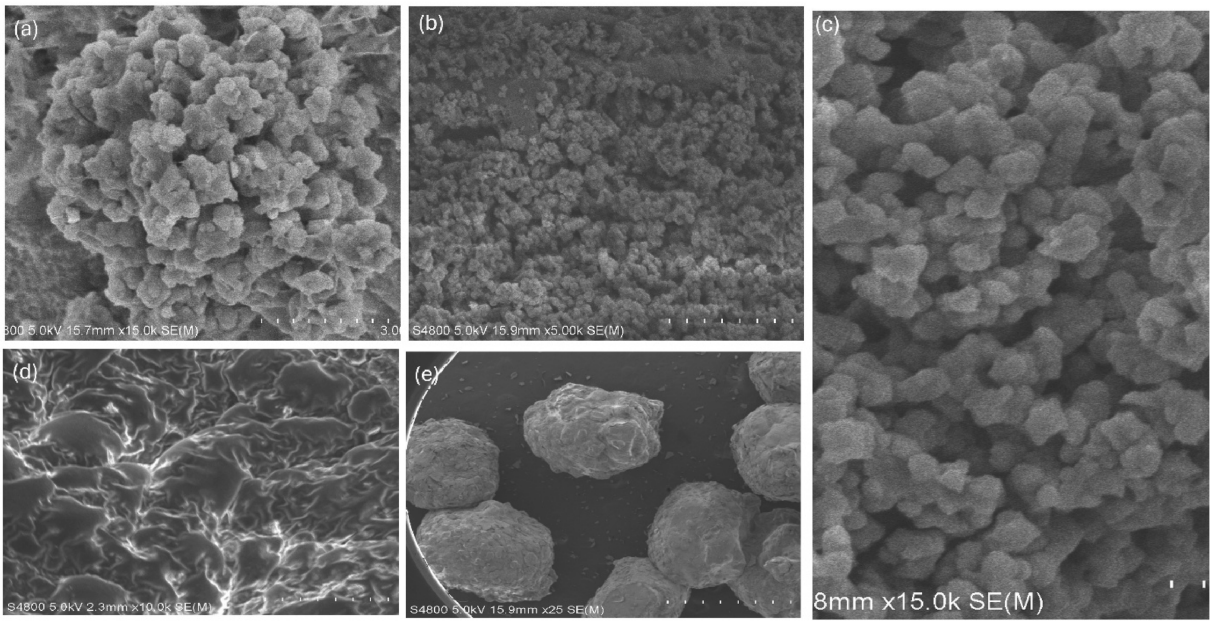

Fig. 3. SEM images of (a) plain Fe-Mn oxides; PAA–chitosan–FeMn composites (b) before dye adsorption and (c) after dye adsorption; (d) surface of chitosan beads; (e) chitosan beads with Fe-Mn oxides.

increases dramatically which may change in the surface configuration. The difference in surfaces before and after adsorption suggests that various adsorption mechanisms were involved on the surface, and this is confirmed from XPS analysis which shows different adsorption mechanisms which resulted in different surface morphologies. These observations confirm that dye adsorption leads to significant changes in surface texture and morphology, supporting the successful uptake of dye molecules and their interaction with the polymer–oxide hybrid structure. The beads were also characterized by SEM analysis (Fig. 3(d) and (e)). The beads have a near-spherical shape with a diameter range of 1–2 mm. However, they are different from those of composite materials (Fig. 3(a)–(c)) with a greater number of irregularities observed on the surface of the beads. The particles have a hollow, micron-sized framework within their internal microstructure, as observed in the cutting plane (Fig. 3(d)) [36]. The overview of beads show that, the shapes of beads were not completely spherical (Fig. 3(e)) [37].

The HR-TEM images of PAA–chitosan–FeMn composite ((a_1)–(a_4)) and HAADF ((b_2)–(b_4)) are presented in Fig. 4. TEM images revealed well-dispersed, quasi-spherical particles embedded within a semi-amorphous polymeric matrix. The microparticles appeared uniformly distributed within the chitosan–PAA framework, indicating effective stabilization by the biopolymer components. Some degree of lattice fringes was observed in HR-TEM, confirming the crystalline nature of the metal oxide domains, while selected area electron diffraction patterns showed a combination of diffuse rings and sharp spots, suggesting a semi-crystalline structure [38]. The HR-TEM images did not reveal distinct crystalline morphologies, but instead showed aggregated, amorphous-like particles, suggesting a disordered nanoscale structure. XPS analysis confirmed the presence of both Fe and Mn, with binding energy values consistent with Fe^{3+}/Fe^{2+} and Mn^{4+}/Mn^{3+} states.

3.1.6. Raman spectroscopy

Raman spectroscopy was utilized to examine the vibrational characteristics and structural composition of the PAA–chitosan–FeMn. The Raman spectrum revealed distinct features corresponding to both the organic polymeric matrix and the inorganic metal oxide components. Strong bands observed in the 500–700 cm^{-1} region were attributed to the M–O stretching vibrations, specifically Fe–O and Mn–O bonds, confirming the formation of iron and manganese oxide phases (Fig. 5(a)). These bands are characteristic of spinel or layered oxide structures and reflect the presence of mixed oxidation states in the composite material. Additional Raman bands near 1350 cm^{-1} (D-band) and 1600 cm^{-1} (G-band) were associated with the disordered and graphitic carbonaceous features of the organic backbone, particularly from the polyacrylic acid and chitosan components. The D-band indicates structural disorder, while the G-band arises from C=C stretching in sp^2-hybridized carbon, suggesting partial interaction or complexation between the polymers and metal oxide domains. Weaker bands in the 2800–3000 cm^{-1} region correspond to C–H stretching vibrations from the aliphatic chains in chitosan and polyacrylic acid. Broadening or overlapping of these bands indicates a highly interconnected polymer–oxide network. The Raman spectral features collectively confirm the successful integration of polyacrylic acid and chitosan with Fe–Mn mixed oxides, forming a composite with both organic functionality and metal oxide characteristics. These vibrational fingerprints provide insight into the material's structure, surface bonding, and potential active sites for adsorption or catalytic activity [39]. After dye adsorption, significant changes were observed in the raman spectra. New peaks appeared or existing bands increased in intensity around 2000–2500 cm^{-1}, corresponding to the vibrational modes of the adsorbed dye molecules (such as aromatic ring stretches, azo –N=N– linkages, or sulfonate groups, depending on the dye). In particular, enhanced signals in the region of 3000 cm^{-1} suggest π–π interactions or coordination between aromatic dye structures and the polymer–oxide framework. Minor shifts in the M–O stretching bands also indicated possible interaction between the dye and surface metal sites. These spectral changes confirm successful dye adsorption onto the composite surface, with both physical and chemical interactions taking place between the dye molecules and the functional groups of the hybrid material.

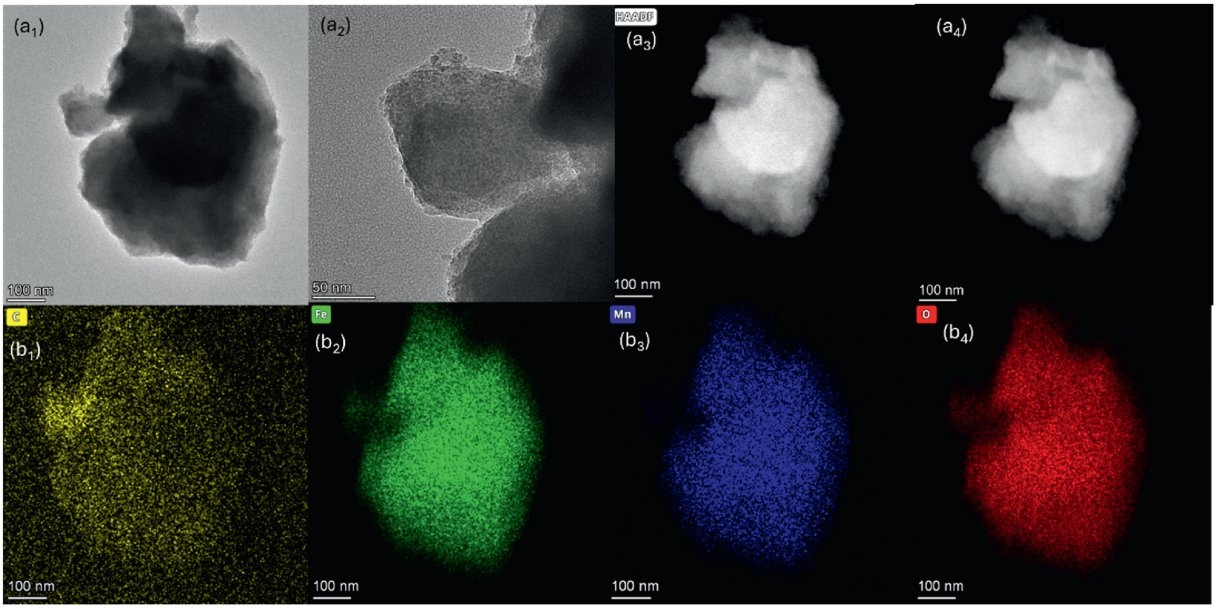

Fig. 4. (a_1)–(a_4) HR-TEM images and (b_1)–(b_4) HAADF images of PAA–chitosan–FeMn composites.

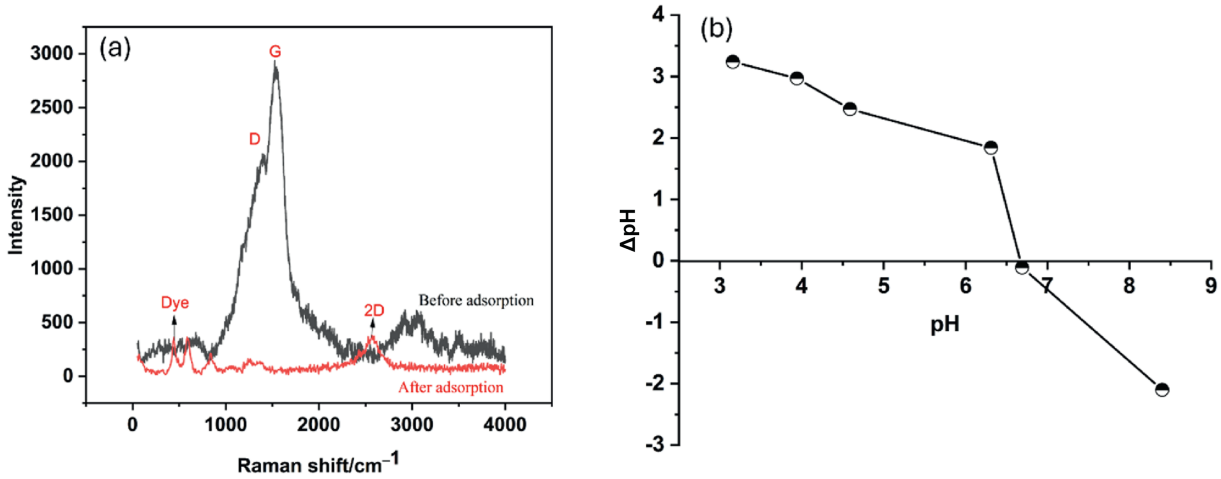

Fig. 5. (a) Raman spectra of PAA–chitosan–FeMn composite before and after dye adsorption; (b) point of zero charge (PZC) of the adsorbent.

3.1.7. AFM analysis

AFM was employed to analyze the surface topography and roughness characteristics of the PAA–chitosan–FeMn composite before and after dye adsorption. Before dye adsorption, the AFM images revealed a relatively rough and heterogeneous surface with distinguishable protrusions (Fig. 6(a_1)–(a_4)). The composite exhibited granular features, consistent with the presence of metal oxide nanoparticles embedded within the polymeric matrix. The average surface roughness (R_a) was relatively high, indicating an open, porous surface favorable for dye interaction. This textured morphology reflects the hybrid nature of the material, combining both organic and inorganic domains. After dye adsorption, AFM images showed a noticeable decrease in surface roughness and a smoother overall topography (Fig. 6(b_1)–(b_4)). The reduction in R_a values suggested that dye molecules had adhered to or partially filled the surface features, reducing the height variation across the surface. In some areas, the topographic profiles appeared flattened, which may be attributed to surface coverage or the formation of a dye–polymer layer. The smoother appearance further supports successful dye adsorption, likely through surface interaction and pore occupation. Overall, AFM analysis confirmed morphological changes at the nanoscale after dye uptake, demonstrating that the adsorption process not only affects chemical composition but also alters the physical surface characteristics of the composite material [40].

3.2. DFT study

To analyze the interaction of azo dyes with PAA stabilized–Fe/Mn–chitosan composite, we chose a simple composite model consisting of doped rings of chitosan and PAA-fragment linked by iron and manganese oxides. The binding energy E_b is defined as

$$E_b = E_{(Composite)} + E_{(CR/RB19)} - E_{(Composite-CR/RB19)} \quad (7)$$

Calculated characteristics of the PAA stabilized–Fe/Mn–chitosan composite with CR and RB 19 azo dyes are presented in Table 1. Fig. 7 presents the atomic structure, HOMO, and LUMO images of

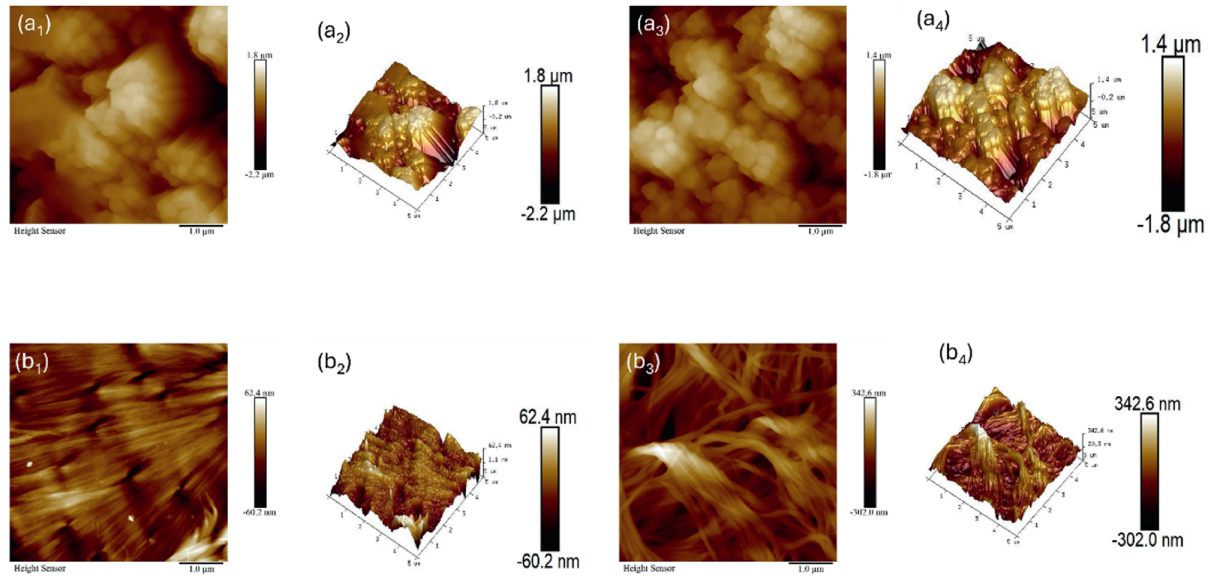

Fig. 6. AFM spectra of PAA–chitosan–FeMn composite (a_1)–(a_4) before adsorption of dye and (b_1)–(b_4) after adsorption of dye.

Table 1
Calculated characteristics of the PAA–chitosan–FeMn composite with CR and RB19 azo dyes.

System	Dipole moment/Debye	HOMO/eV	LUMO/eV	η/eV	χ/eV	E_b/eV
PAA–chitosan–FeMn composite	12.429	−5.587	−5.116	0.471	5.351	–
CR/PAA–chitosan–FeMn composite	13.941	−5.369	−4.550	0.819	4.959	1.885
RB19/PAA–chitosan–FeMn	6.928	−0.486	−4.969	0.517	5.227	1.176

CR/composite model. Fig. 8 presents the same images for RB19/composite model. One of the most important parameters used for the analysis of the chemical interactions is the chemical hardness [41]. This parameter is defined as the resistance against polarization of molecular and atomic chemical systems. The close relation between chemical hardness and stability is given through maximum hardness principle [42]. This principle states that "there seems to be a rule of nature that molecules arrange themselves so as to be as hard as possible". This statement implies that hard chemical systems will exhibit high stability. The fact that the binding energy of the chemical system of CR/composite is higher than the value obtained for the energy of RB19/composite can be explained by chemical hardness. It is already expected that the hardness and therefore the stability will be higher in the system where the binding energy is high. From the obtained data it follows that CR is attached to the composite stronger than RB19. From the data presented in Table 1, it is evident that the total dipole moment drops significantly when RB19 is attached to the composite. At the same time, the HOMO–LUMO gap slightly increases. The HOMO–LUMO gap for the system containing CR is higher than for the composite with RB19.

3.3. Kinetic study

The adsorption kinetics of azo dyes were studied to elucidate the factors governing the rate of adsorption, providing valuable insights into the underlying mechanisms that control the adsorption process. This method can be effectively explored for wastewater treatment if the estimated contact time required for the adsorption process is relatively short. Kinetic parameters were investigated at pH 9 and for CR and pH 5 for BR19 at various temperatures (298–328 K) at 50 mg·L^{-1} concentration over 24 h. The dye adsorption process on PAA–chitosan-FeMn composite was rapid in the beginning afterwards, Adsorption capacity increased slowly until equilibrium was reached. After equilibrium the adsorption was constant, as the composite material becomes saturated with dye molecules, the active binding sites start releasing the dye back into the solution, so that the addition of time no longer increases the adsorption of CR and BR19 azo dyes. The plot of dye quantity adsorbed versus time in Fig. 9(a) and (b) illustrates the adsorption process reaching equilibrium, where no further adsorption occurs. The data indicates that the adsorption process reached equilibrium within 20 min for CR (Fig. 9(a)) and 50 min for BR19 (Fig. 9(b)). The adsorption rate was high in the beginning and became constant after reaching equilibrium. The adsorption of BR19 was found to be more than that of CR because of the double azo structure of CR which is more complex than BR19 and diffusion in case of CR is slow as compared to BR19. Moreover, it also may be due to more affinity of surface towards BR19 azo dye. This suggests that once the adsorption equilibrium is reached, extending the contact time does not lead to further significant removal of the dye. It is obvious from the figures that the adsorption decreases with temperature in case of BR19 while a little change was observed in case of CR adsorption. The observation confirms that the adsorption process is exothermic, meaning it releases heat. The low adsorption at high temperature was due to active sites destruction at high temperature. Although the amine/carboxyl functionalized Fe–Mn mixed oxide composite initially shows strong adsorption of both azo dyes at 298 K, a gradual decline in capacity is observed after equilibrium because at equilibrium, adsorption and desorption occur simultaneously. For dual-charged systems, weakly bound dye molecules may desorb back into solution once surface saturation is reached. This leads to a net reduction in apparent adsorption capacity over time. Another reason may be non-covalent interactions such as hydrogen bonding and $\pi-\pi$ stacking contribute to adsorption but

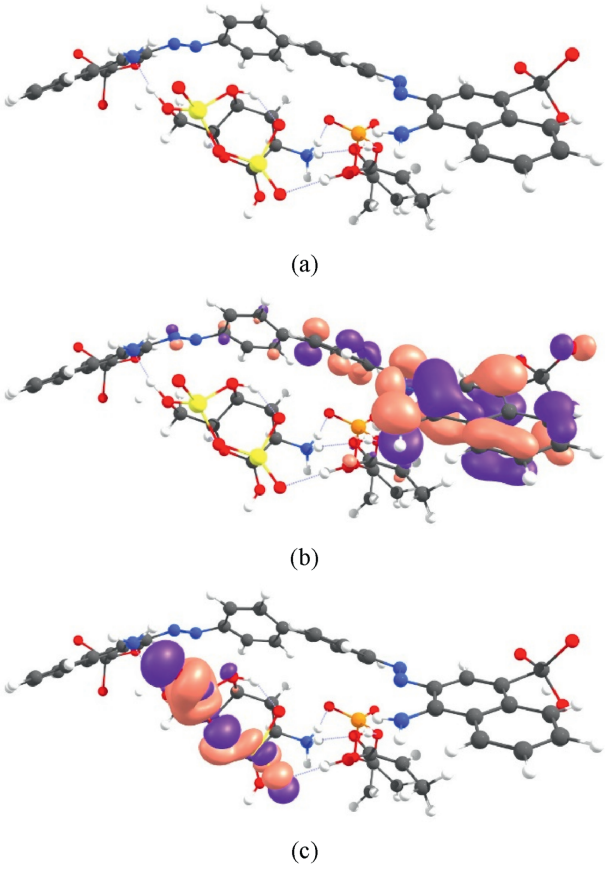

Fig. 7. CR/PAA–chitosan–FeMn composite models: (a) atomic structure, (b) HOMO, and (c) LUMO.

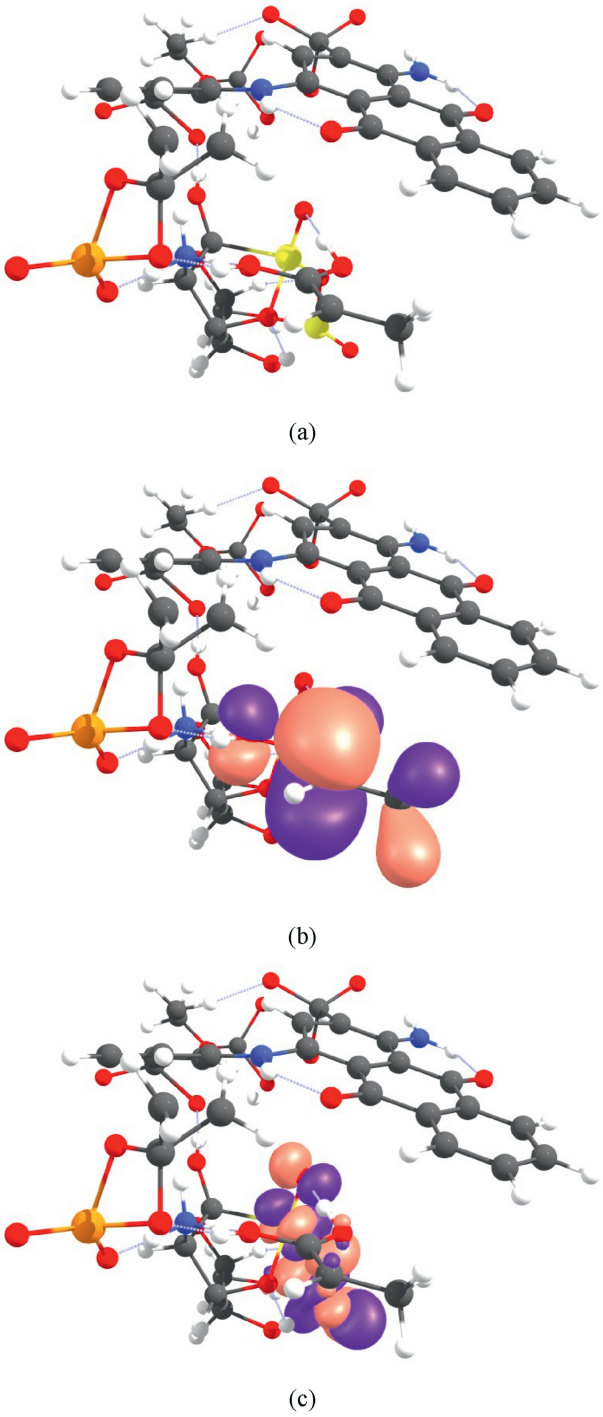

Fig. 8. RB19/PAA–chitosan–FeMn composite models: (a) atomic structure, (b) HOMO, and (c) LUMO.

are relatively unstable over time at ambient conditions. Once equilibrium is reached, these interactions may relax, leading to slow desorption of dye molecules.

Pseudo-first-order and pseudo-second-order kinetic models are commonly used to study dye molecule adsorption mechanisms onto various adsorbent materials [43].

The pseudo-first-order kinetic model is often expressed as:

$$\frac{1}{q_t}=\frac{1}{q_e}+\frac{k_1}{q_e t} \tag{8}$$

where q_e ($mg\cdot g^{-1}$) is the equilibrium adsorption capacity, and q_t ($mg\cdot g^{-1}$) is the adsorption capacity at time t, k_1 is the pseudo-first-order rate constant. The values can likely be calculated from the slope and intercept of the graph $1/q_t$ *vs.* $1/t$ (not shown). The pseudo-first-order model doesn't fit well, as the calculated q_e value deviates from experimental data. The pseudo-second-order equation is typically written as:

$$\frac{t}{q_t}=\frac{1}{k_2 q_e^2}+\frac{t}{q_e} \tag{9}$$

where q_t is the adsorption capacity at time t and q_e is the equilibrium adsorption capacity, and k_2 represents the rate constant. The linear plot of t/q_t *vs.* t in Fig. 9(c) and (d) and the close agreement between experimental and calculated q_e values, along with R^2 values near unity (Tables 2 and 3) suggest that the pseudo-second-order model accurately describes the adsorption kinetics of the dyes. The higher k_2 values for BR19 compared to CR indicate faster adsorption kinetics for BR19. This study's experimental data demonstrated superior fitting (with $R^2 > 0.999$) to the pseudo-second-order model in contrast to the pseudo-first-order model, indicating that chemisorption predominates the rate-limiting step in both dyes adsorption. Chemisorption is strong chemical bonds between the dye molecule and adsorbent surface typically result in high adsorption capacities and more permanent adsorption [43].

The intraparticle diffusion model helps understand the adsorption mechanism and identify rate-controlling steps. The linear form of the intraparticle diffusion model is typically represented as:

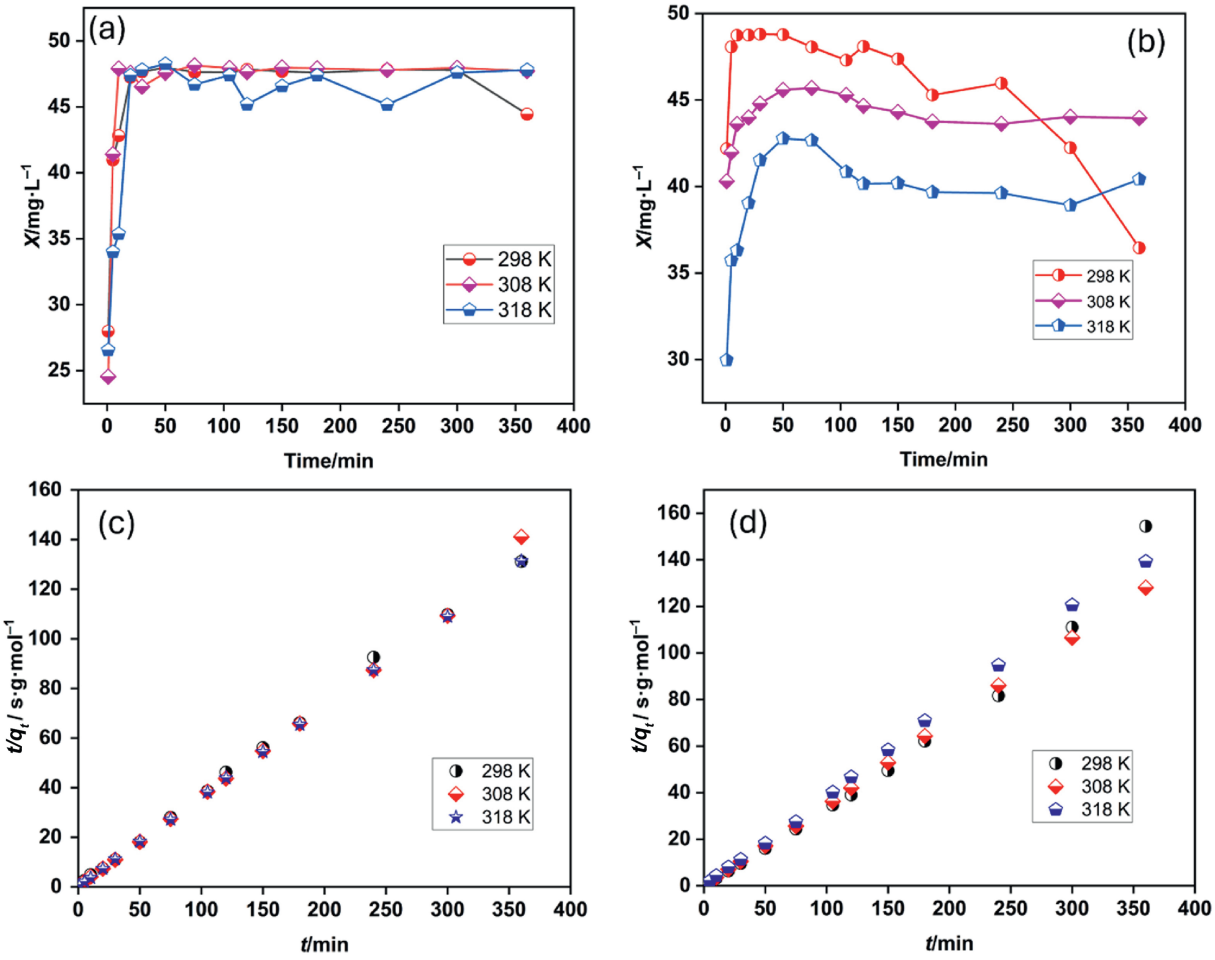

Fig. 9. Kinetics of (a) CR, (b) BR19 and pseudo second order plot for (c) CR, (d) BR19 onto PAA–chitosan–FeMn composite at 50 mg·L^{-1} concentration.

Table 2
Pseudo second-order parameters for CR adsorption at pH 9 at 50 mg·L^{-1}.

Temperature/K	k_2	Experimental, x/mg·g^{-1}	Theoretical, x/mg·g^{-1}	R^2
298	0.031	19.12	18.97	0.999
308	0.026	19.06	18.45	0.997
318	0.160	19.16	19.15	1.000

Table 3
Pseudo second-order parameters for BR19 adsorption at pH 9 at 50 mg·L^{-1}.

Temperature/K	k_2	Experimental, x/mg·g^{-1}	Theoretical, x/mg·g^{-1}	R^2
298	0.041	19.51	15.79	0.98
308	0.056	18.27	17.54	0.99
318	0.057	17.10	15.87	0.99

$$q_t = K_d\, t^{1/2} + C \tag{10}$$

where q_t is the amount adsorbed at time t, K_d is the intraparticle diffusion rate constant, and C is the intercept related to boundary layer thickness. Özacar and Şengil [44] also observed this types of multilinearity graphs for complex yellow sorption onto pin sawdust at 298 K. The study highlights a two-stage adsorption process: an initial external diffusion stage followed by a gradual intraparticle diffusion stage, with the latter being the rate-controlling step. If the plot of q_t *versus* $t^{1/2}$ passes through the origin and exhibits linearity, it indicates that intraparticle diffusion is the rate-determining step in the adsorption process. The deviation from the origin in Fig. 10(a) and (b) suggests that pore diffusion is not the sole rate-controlling step in the adsorption process. The deviation is attributed to the varying transfer rates observed during the initial and final stages of the adsorption process. The R^2 values in Tables 4 and 5 support the intraparticle diffusion model for both dyes. However, the lines not passing through the origin due to intercept C indicate a boundary layer effect, suggesting intraparticle diffusion isn't the sole rate-controlling step [45] (see Fig. 11).

The Boyd model helps identify the actual rate-determining step in adsorption processes.

The Boyd model equation is typically given as:

$$F = 1 - \left(\frac{6}{\pi^2}\right)\sum_{m}^{1}\left(\frac{1}{m^2}\right)\exp\left(-m^2 Bt\right) \tag{11}$$

where F is the fraction of solute adsorbed at time t by following relation

$$F = \frac{q_t}{q_e} \tag{12}$$

Eq. (11) can be expressed as:

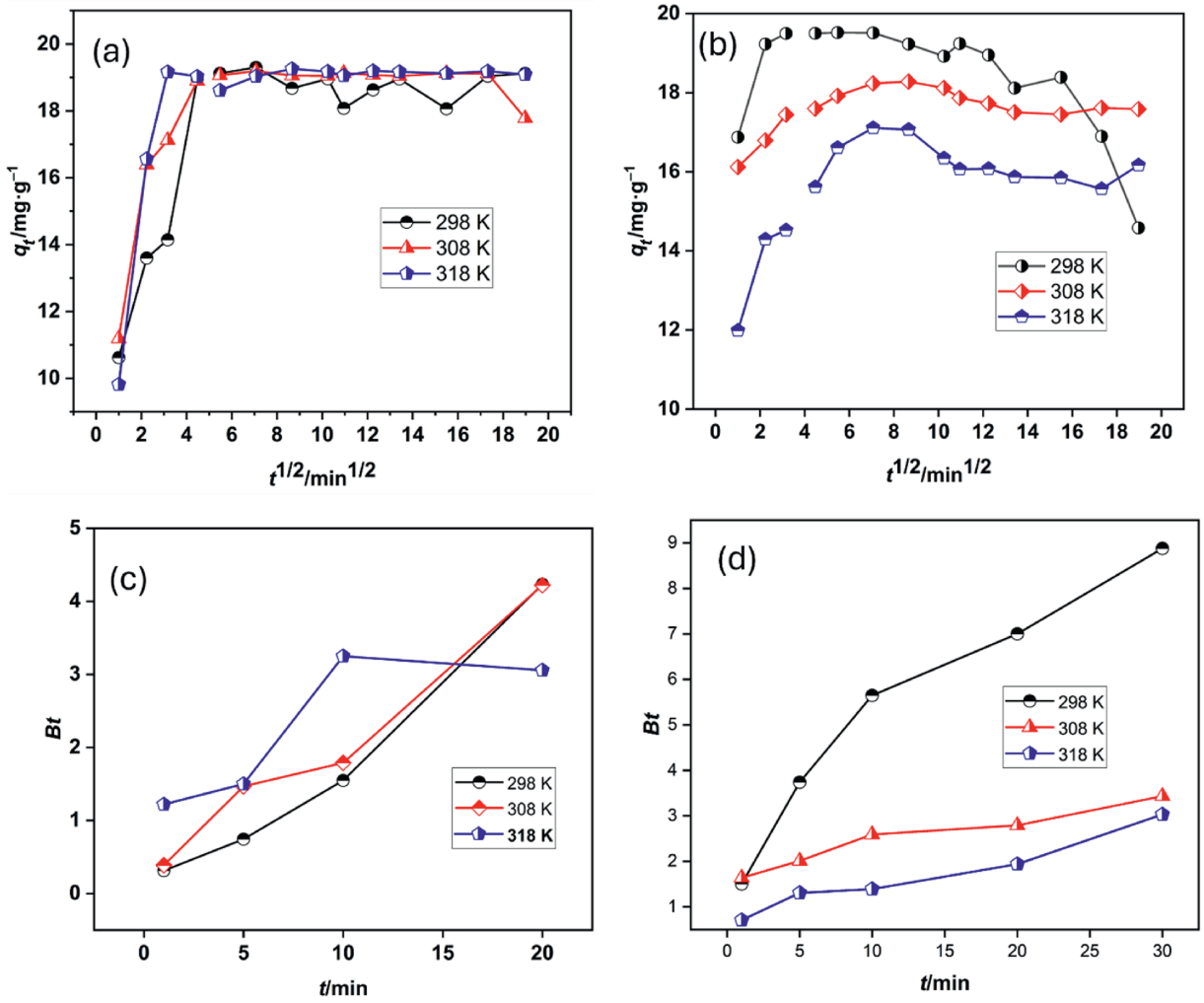

Fig. 10. Intraparticle diffusion plots for (a) CR, (b) BR19 and Boyd plot for (c) CR, (d) BR19 on PAA–chitosan–FeMn composite at 50 mg·L^{-1}.

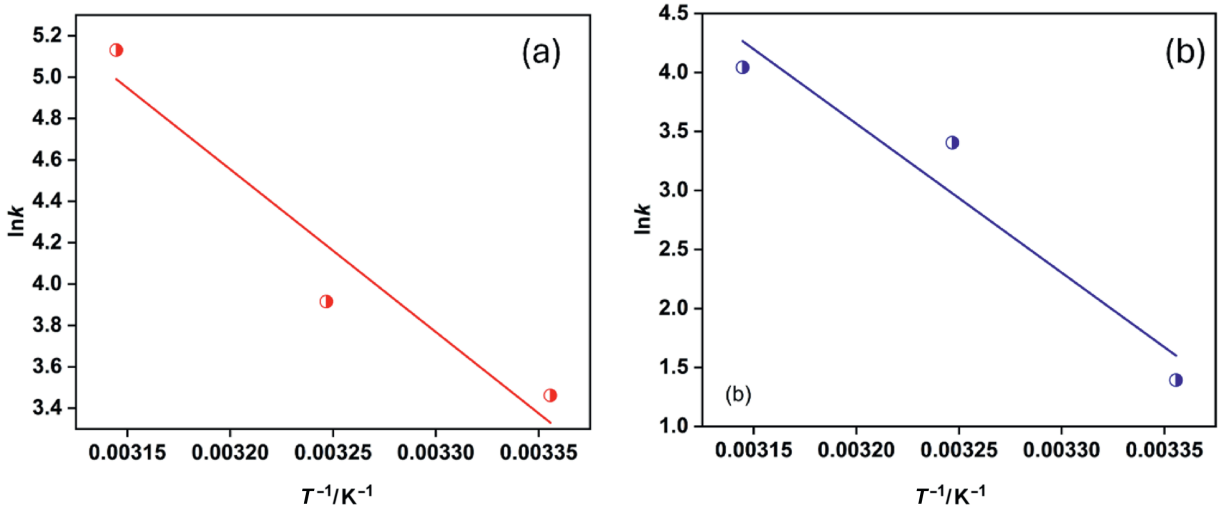

Fig. 11. Arrhenius plots for (a) CR adsorption and (b) BR19 adsorption.

Table 4
Intraparticle model parameters for CR at 50 mg·L^{-1}.

Temperature/K	K_d/mg·g^{-1}·min$^{-0.5}$	R^2
298	1.67	0.94
308	2.82	0.89
318	4.38	0.97

Table 5
Intraparticle model parameters for BR19 at 50 mg·L^{-1}.

Temperature/K	K_d/mg·g^{-1}·min$^{-0.5}$	R^2
298	1.24	0.91
308	0.60	0.99
318	1.20	0.89

Table 6
Arrhenius parameters for CR and BR19 adsorption at 50 mg·L^{-1}.

Dye	E_a/kJ·mol^{-1}	R^2
CR	65.33	0.925
BR	104.98	0.927

$$F \text{ values } > 0.85\ Bt = -0.4977 - \ln(1 - F) \tag{13}$$

and for

$$F \text{ values } < 0.85\ Bt = \left[\sqrt{\pi} - \sqrt{\pi - \frac{\pi^2 F}{3}}\right]^2 \tag{14}$$

where q_e is adsorption at equilibrium, q_t is adsorption at time t, F is the fraction of solute adsorbed at time t, and Bt is a mathematical function of F. Fig. 10(c) and (d) show that the plots did not pass through the origin, which confirms that the adsorption is mostly controlled by external diffusion (film diffusion) [46].

The temperature dependence of the adsorption rate constant can be elucidated using models like the Arrhenius equation, which helps determine activation energy and understand the adsorption mechanism., which is expressed as:

$$\ln k = \ln A - \frac{E_a}{RT} \tag{15}$$

where k is rate constant, A is the pre-exponential factor, E_a is activation energy, R is the gas constant, and T is the temperature in Kelvin. By plotting ln$k$ *vs.* 1/T, the activation energy (E_a) can be calculated from the slope ($-E_a/R$) and the pre-exponential factor (A) from the intercept. The linear plot of ln$k$ *vs.* 1/T allowed calculation of activation energies for CR and BR19 adsorption onto PAA–chitosan–FeMn composite, which were 65.33 and 104.98 kJ·mol^{-1}, respectively (Table 6). The activation energy provides insight into the nature of the adsorption process, distinguishing between physical and chemical adsorption. If adsorption process occurs with low activation energy (0–120 kJ·mol^{-1}) it means that adsorption has physical nature and if adsorption occurred with high activation energy (120–400 kJ·mol^{-1}) it means that adsorption has chemical nature. Similar results were obtained by Ref. [47] during adsorption of azo and anthraquinones dyes onto artificial keratin fibers.

3.4. Effect of various parameters

3.4.1. Effect of initial concentration

The initial adsorbate concentration affects the adsorption process by altering the availability and accessibility of binding sites on the adsorbent surface. The relationship between initial dye concentration and percentage removal can vary depending on the adsorption system. Sometimes, higher initial concentrations can lead to lower percentage removal due to saturation of adsorption sites. The study examined how various concentrations (5–200 mg·L^{-1}) of CR and BR19 dyes affected their adsorption by PAA–chitosan–FeMn composite, using a fixed adsorbent dose of 0.1 g. It could be seen from Fig. 12(a) that the percent removal was increased because dye molecules are settled in the active sites at lower concentration. Higher dye concentrations lead to more dye molecules competing for limited adsorption sites, resulting in equilibrium being reached sooner, potentially limiting overall adsorption capacity. At higher dye concentrations, the mass transfer resistance is overcome, allowing more efficient adsorption. Conversely, lower concentrations result in many unoccupied active sites, decreasing overall adsorption capacity. The mass transfer resistance between the liquid (dye solution) and the solid adsorbent is significantly overcome by the higher starting concentration [48]. Increasing the initial dye concentration enhances the mass transfer driving force, resulting in higher adsorption onto the available binding sites of the PAA–chitosan–FeMn composite and at higher dye concentrations (above 100 mg·L^{-1}, especially 200 mg·L^{-1}), the ratio of dye molecules to available binding sites becomes unfavorable, hindering mass transfer. Similar results were reported by Khan *et al.* [10] while studying MgO composite for dye adsorption.

3.4.2. Effect of pH

pH influences the adsorbent surface charge and the pollutant protonation state, impacting adsorption efficiency, influencing adsorption efficiency [49]. The adsorption of dye by PAA–chitosan–FeMn composite was studied in pH ranges from 3 to 11 at 298 K. The study used 0.1 g of adsorbent and an initial concentration of 50 mg·L^{-1} to investigate adsorption process. The point of zero charge (PZC) of the prepared materials was found to be in the range of 6.5–6.8 (Fig. 5(b)). At pH values below 6.5, the surface of the adsorbent becomes positively charged due to protonation of surface hydroxyl groups (M–OH_2^+). Around pH 6.5–6.8, the surface charge is nearly neutral. Electrostatic interactions are minimized, so adsorption mainly depends on specific interactions such as hydrogen bonding, π–π interactions, or complexation with polymer functional groups. The adsorption efficiency may be moderate compared to strongly acidic or basic conditions. pH values above 6.8, the surface becomes negatively charged due to deprotonation of hydroxyl groups (M–O^-). In the current study the irregular pH effect is due to the other adsorption mechanism instead of electrostatic attraction such is hydrogen bonding, π–π interactions and interaction with polymer functional groups.

At pH 3, excessive H^+ protonates COO– and –NH_2 groups on the adsorbent, forming –COOH and –NH_3^+, reducing adsorption sites for CR. Similarly, at pH 11, the adsorption decreases likely due to changes in dye or adsorbent charge. Meanwhile, H^+ ions competed with dye ions for adsorption sites, reducing dye adsorption efficiency. When the pH increased gradually, the adsorbent was deprotonated on –NH^{4+} and –COOH, and many –NH_2 and –COO^- chelate with dyes ions, so that the adsorbent increased the adsorption of dyes ions. Under strong alkaline conditions, increased ionic strength reduces osmotic pressure difference, shrinking the adsorbent network and decreasing adsorption capacity [50]. In the case of BR19 it was evident that the percent removal of RB19 was maximum at acidic pH (pH 3) (Fig. 12(b)) and decreased with further increase in pH though up to a pH of 5. In alkaline conditions, repulsion between negatively charged sulfonic groups on dye molecules and carboxyl groups on the adsorbent

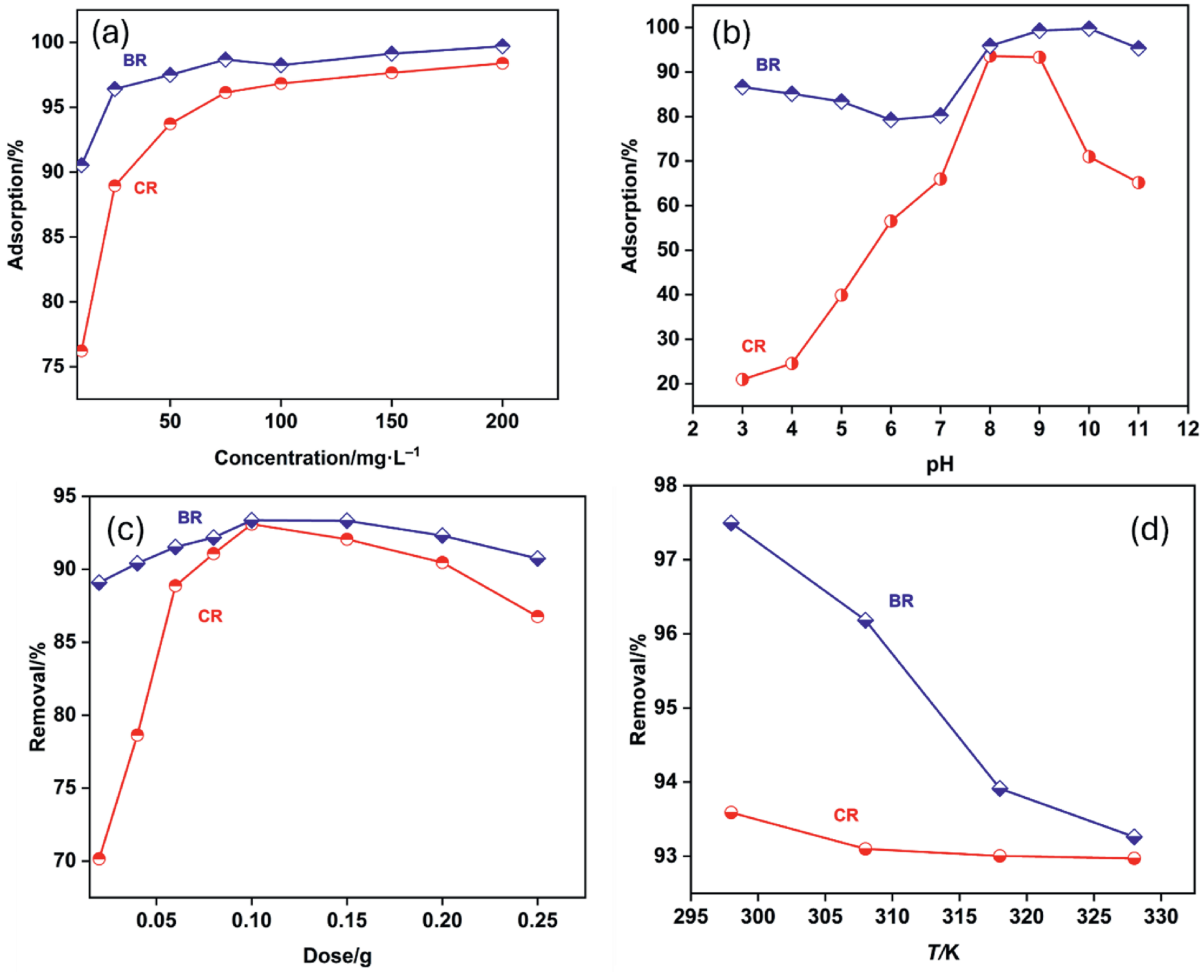

Fig. 12. Effects of (a) initial concentration (5–200 mg·L^{-1}), (b) pH (3–11), (c) adsorbent dosage (0.05–0.25 g), and (d) temperature (298–328 K), of CR and BR19 adsorption onto PAA–chitosan–FeMn composite.

likely reduces adsorption efficiency [48]. Moreover, at alkaline pH lower removal of both dyes was attributed to excess OH ions, thus competing the sorption in the active sites of the adsorbent.

The Fe–Mn mixed oxide core exposes amphoteric surface hydroxyls (M–OH; M = Fe, Mn) that protonate/deprotonate with pH:

Acidic: $M{-}OH + H^+ \rightleftharpoons M{-}OH_2{}^+$

Basic: $M{-}OH \rightleftharpoons M{-}O^- + H^+$

The grafted polymer shell contributes amine ($-NH_2/-NH_3{}^+$) and carboxyl ($-COOH/-COO^-$) groups. Around the measured PZC = 6.5–6.8, both positive ($-NH_3{}^+$, $M{-}OH_2{}^+$) and negative ($-COO^-$, $M{-}O^-$) sites coexist yielding a dual-charged interface that presents complementary binding domains without pore collapse or polymer swelling. Adsorption capacity of this adsorbent has been compared with other reported literature (Table 7).

3.4.3. *Effect of dose*

The adsorbent dose is a critical parameter that determines the adsorption capacity of the adsorbent at a fixed temperature and initial dye concentration. The study investigated azo dye absorption by varying adsorbent dosage (0.05–0.25 g) in a 50 mg·L^{-1} dye solution. The study examines how varying adsorbent dosage affects dye removal percentage, keeping initial dye concentration (50 mg·L^{-1}) and contact time (120 min) constant [51]. Fig. 12(c)

Table 7
Comparison of adsorption capacity with reported adsorbents.

Adsorbent	Dye	Conditions (conc., dose, pH, time)	Removal/%	Limitation	References
Sawdust (untreated)	Congo red	Neutral pH	68.9	Low surface area, slow kinetics	[55]
Ulva sp. membrane	Congo red	50–100 mg·L^{-1}; 240 min	~79.6	Natural algae fiber, limited porosity	[56]
$NiFe_2O_4$ nanofibers	Congo red	100 mg·L^{-1}; 240 min	65	Lower adsorption due to fewer active sites	[57]
Fly ash	Congo red	pH ~7	~40–50	Very low capacity (22 mg/g)	[58]
Yeast biomass	Reactive blue-19	pH 6	50	Slow kinetic	[59]
Nylon-6 nanofiber	Reactive blue-19	Acidic pH	~61	Limited surface functionality	[60]
Nano-carbon	Reactive blue-19	50–200 mg·L^{-1}	~79.5	Below 80% under certain equilibrium states	[61]
PAA–chitosan–FeMn	Congo red	pH 8	95	–	This study
PAA–chitosan–FeMn	Reactive blue-19	pH 10	99.7	–	This study

shows that increasing the adsorbent dosage from 0.05 g to 0.1 g enhances dye removal percentage, and remains constant from 0.1 to 0.25 g of adsorbent. The increased adsorption observed between 0.05 and 0.1 g of adsorbent is attributed to the availability of additional binding sites. However, beyond 0.1 g, the agglomeration of adsorbent particles occurs, resulting in a decrease in adsorption. The study optimized the adsorbent dose at 0.1 g. Similar findings were reported by Khan *et al.* [52] during adsorption of methyl orange and congo red by PVP–MnO_2 composite.

3.4.4. Effect of temperature

Temperature is a pivotal parameter that profoundly impacts the adsorption process, exerting significant influences on both its kinetic and thermodynamic aspects. The study investigates the impact of temperature on adsorption, covering a range from 298 to 328 K (Fig. 12(d)). The study found that increasing temperature (298–328 K) decreased dye removal for BR19 and slightly decreased adsorption for CR. The negative correlation between temperature and adsorption capacity confirms that the process is exothermic, consistent with the release of energy upon dye uptake. Increasing temperature shifts the adsorption equilibrium toward desorption, thereby lowering dye retention on the surface. The amine ($-NH_2$) and carboxyl (−COOH) groups provide dual-charged adsorption sites that can simultaneously interact with oppositely charged dyes. However, at higher temperatures, partial deprotonation/protonation equilibrium shifts can reduce the availability of charged sites, thereby diminishing adsorption efficiency. At lower temperatures, the composite surface provides energetically favorable sites for dye uptake, facilitated by electrostatic attraction between the oppositely charged functional groups ($-NH_2^+/-COO^-$) and dye molecules, as well as secondary interactions such as hydrogen bonding and π–π stacking. High temperature imparts additional kinetic energy to dye molecules, which disrupts electrostatic and hydrogen-bonding interactions between the functionalized surface and dye molecules. This weakens the affinity of the composite surface toward both cationic and anionic dyes. These findings are further substantiated by DFT studies, which reveal that dye–composite interactions involve strong localized binding through functional group coordination and electrostatic pairing. The calculated adsorption energies decrease with simulated thermal excitation, consistent with experimental desorption trends at elevated temperatures [53].

3.4.5. Multicomponent removal studies of CR, BR and MB by PAA–chitosan–FeMn composite

To evaluate the multifunctional adsorption capability of the PAA–chitosan–FeMn composite, 0.3 g of the adsorbent was added to 120 ml of a mixed dye solution containing CR, RB19, and MB at 298 K for 120 min. Upon reaching equilibrium, the disappearance of color from the solution confirmed the effective removal of all dyes. These results clearly demonstrate the composite's strong affinity for both anionic and cationic contaminants, highlighting its potential as a versatile and efficient adsorbent for wastewater treatment applications.

3.4.6. Regeneration study

The practical application of an adsorbent strongly depends on its ability to be regenerated and reused without significant loss in performance. Therefore, the regeneration of the dual-charged, non-swelling composite was systematically investigated using 0.1 $mol \cdot L^{-1}$ HCl solution as the desorbing agent for CR dye. The recovery test was repeated for six cycles and the results are evaluated. The adsorption capacities of adsorbent decrease for every new cycle. The maximum adsorption capacity for CR was found to be 94%. After six cycles, the adsorption capacity dropped to 60%. The results revealed that the composite retained a significant portion of its adsorption capacity over successive cycles, highlighting its structural stability and robustness of the amine/carboxyl functional groups. However, a gradual decrease in removal efficiency was observed with each regeneration step due to the incomplete desorption of dye molecules, partial deactivation of dual-charged sites and thermal and chemical stress during drying and acid treatment. Importantly, the observed regeneration behavior aligns with the thermodynamic nature of the system. Since the adsorption was established as exothermic, higher temperatures already reduce adsorption efficiency, and the regeneration conditions further favor desorption at elevated proton concentrations. DFT calculations corroborate these findings, indicating that although dye molecules strongly interact with amine/carboxyl-functionalized sites, the adsorption energy decreases when the system is exposed to acidic regeneration conditions. This facilitates partial desorption but may also weaken specific binding sites over multiple cycles [54].

3.5. Adsorption isotherms

The Langmuir and Freundlich adsorption isotherms are two prominent mathematical models that describe the equilibrium relationship between the concentration of the adsorbate and the amount of adsorbate adsorbed by the adsorbent.

The linearized Langmuir adsorption model is often expressed as:

$$\frac{C_e}{X} = \frac{1}{K_b X_m} + \frac{C_e}{X_m} \tag{16}$$

where C_e is equilibrium concentration, X_m is maximum adsorption, X ($mg \cdot g^{-1}$) is adsorbed amount, K_b is binding energy constant. The R^2 values showed that Langmuir adsorption model does not application to the current experimental data.

Both adsorption and multilayer sorption occur on heterogeneous surfaces, as postulated by the Freundlich adsorption isotherm, which is expressed as:

$$\lg q_e = \lg K_F + \frac{1}{n} \lg C_e \tag{17}$$

where C_e is equilibrium concentration, q_e is amount adsorbed at equilibrium, Freundlich constant, K_F ($mg \cdot g^{-1}$). n is Freundlich exponent (adsorption intensity). The linear plot of $\lg q_e$ *vs.* $\lg C_e$ allows estimation of Freundlich constants K_F and n from the intercept and slope, respectively (Table 8).

The Dubinin–Radushkevich (DR) isotherm is used to analyze adsorption data, often expressed as:

$$\ln X = \ln q_e X_m - K\epsilon^2 \tag{18}$$

where X is amount adsorbed at equilibrium, X_m is maximum adsorption capacity, q_e is amount adsorbed at equilibrium ($mg \cdot g^{-1}$), ϵ is Polanyi potential which is equal to $RT \ln(1 + 1/C_e)$, K is energy constant. These models estimate adsorption energy, revealing whether adsorption occurs *via* physisorption or chemisorption. A plot of ln*x* *vs.* ϵ^2 gives a linear relationship with high

Table 8
Freundlich parameters for CR and BR19 adsorption onto PAA–chitosan–FeMn composite at 298 K.

Dye	K_F	$1/n$	R^2
CR	0.049	9.08	0.95
BR19	11.51	2.296	0.96

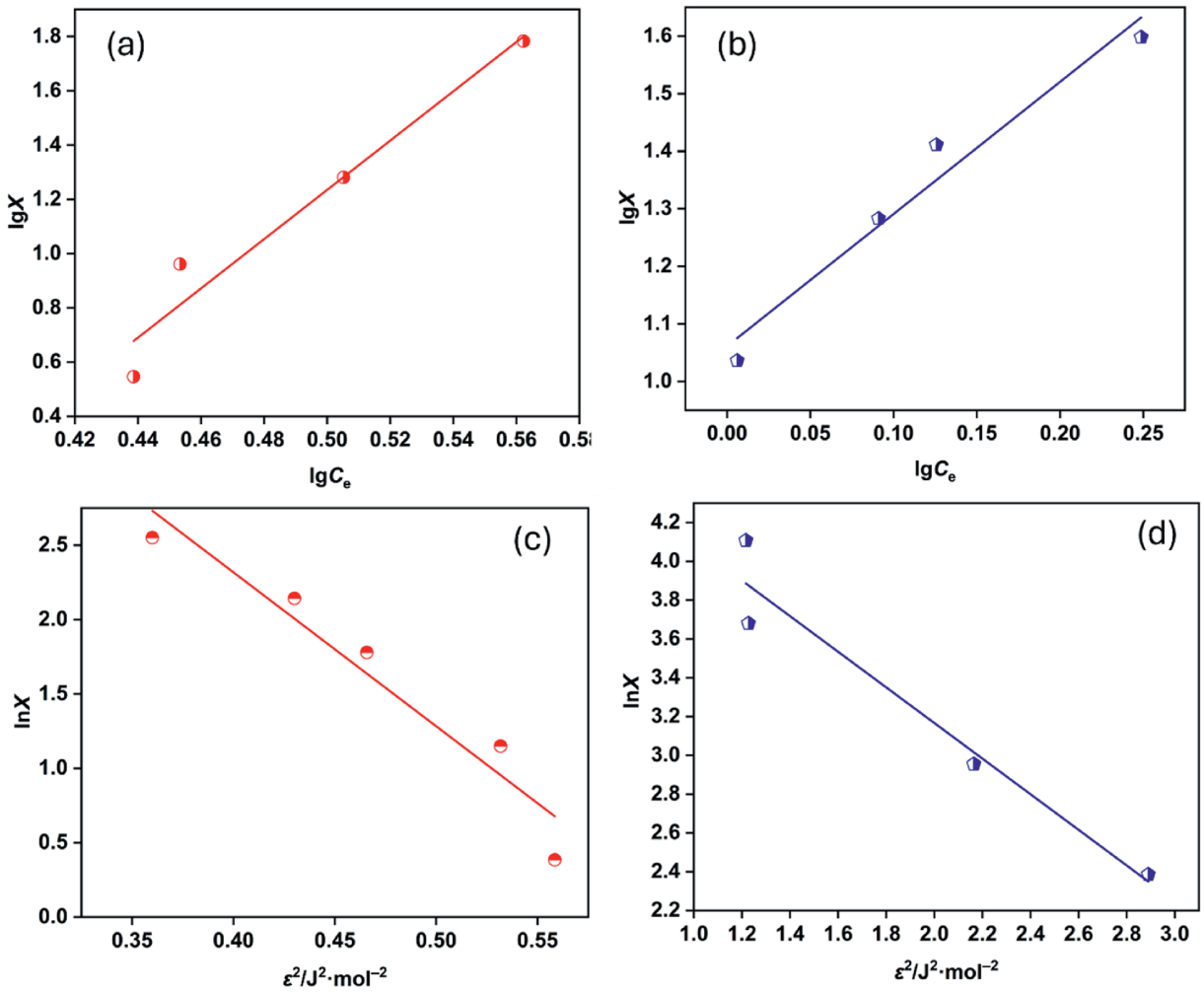

Fig. 13. Freundlich isotherms for (a) CR and (b) BR19; DR plot for (c) CR and (d) BR19 adsorption by PAA–chitosan–FeMn composite.

correlation coefficients (Fig. 13(c) and (d)). The k_d values are used to calculate the mean free energy (E)

$$E = -(2k)^{-0.5} \tag{19}$$

Eq. (19) was applied to find the E. The mean adsorption energy was 0.219 for CR while 0.738 kJ·mol^{-1} for BR19, giving information regarding the mechanisms of the process. Adsorption is considered physical when $E < 8$ kJ·mol^{-1} and chemical when E ranges from 8 to 16 kJ·mol^{-1}. The adsorption process is confirmed to be physical in nature, given the E values are less than 8 kJ·mol^{-1} for both cases, as indicated in Table 9.

3.6. Thermodynamics study

Thermodynamic parameters like ΔG, ΔH, and ΔS help determine the spontaneity and nature of adsorption. ΔG indicates spontaneity, ΔH suggests exothermic or endothermic nature, and ΔS reveals entropy changes. These values were calculated from following relationship

$$K_c = \frac{X}{C_e} \tag{20}$$

$$\ln K_c = \frac{\Delta S}{R} - \frac{\Delta H}{RT} \tag{21}$$

where K_c is constant. The Gibbs free energy (ΔG) was calculated from Eq. (12)

$$\Delta G = \Delta H - T\Delta S \tag{22}$$

The changes in entropy (ΔS) and enthalpy (ΔH) for CR and BR19 were calculated from the plot of ln(K) *vs.* 1/T (Fig. 14(a) and (b)). Negative ΔG values indicate a spontaneous adsorption process (Tables 10 and 11). The lower negative value of ΔG is observed for CR as compared to BR19, confirming that CR adsorption is energetically less favorable. The positive values of ΔS (11.61 and 75.9 J·mol^{-1}·K^{-1}) for CR and BR19 respectively, were due to the high randomness which confirms a good affinity of dyes towards the surface. The positive ΔS values indicate increased randomness or disorder at the solid-solution interface, suggesting that the dye molecules arrange more randomly during adsorption. The negative ΔH values in both cases confirm an exothermic nature of the adsorption process.

3.7. Fixed-bed column studies

The adsorption of CR and BR19 from aqueous media was carried out in continuous fixed-bed column system with a fixed rate of flow (10 ml·min^{-1}) of solution, bed length (0.2 cm) and concentration of the dye (50 mg·g^{-1}). The breakthrough curve observed for CR was 600 min while for BR 720 min for (50 mg·g^{-1}) concentration (Fig. 15). Our previous work

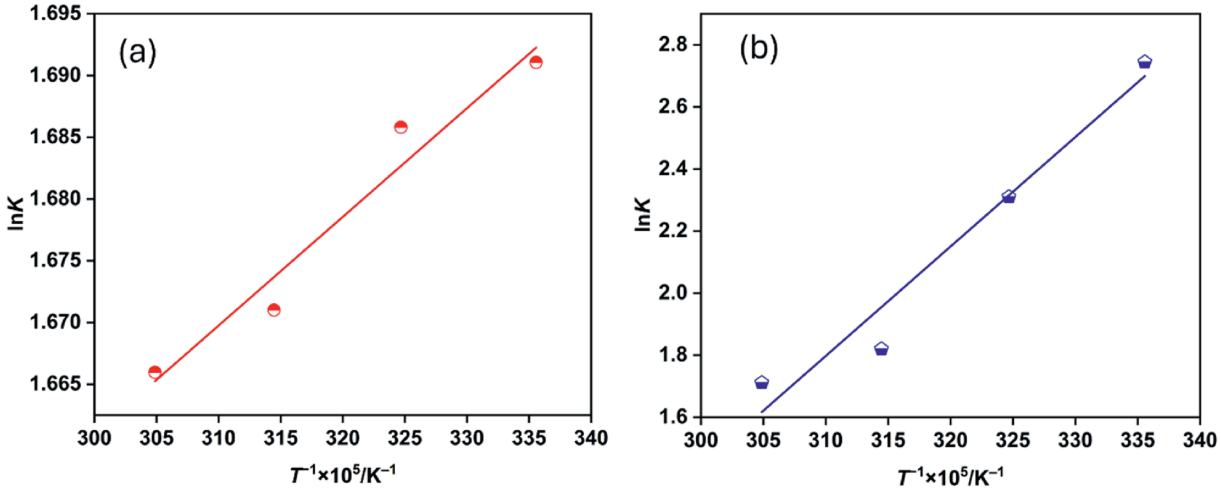

Fig. 14. ln*K* *versus* T^{-1} for (a) CR, and for (b) BR19 onto PAA–chitosan–FeMn composite at 50 mg·L^{-1}.

Table 9
D.R parameters for CR and BR19 adsorption onto PAA–chitosan–FeMn composite at 298 K.

Dye	*E*/kJ·mol^{-1}	R^2
CR	0.219	0.93
BR	0.738	0.94

Table 10
Thermodynamic parameters of CR adsorption onto PAA–chitosan–FeMn composite.

Temperature/K	Δ*G*/kJ·mol^{-1}	Δ*H*/kJ·mol^{-1}	Δ*S*/J·mol^{-1}·K^{-1}
298	−-4.19		
308	−4.30		
318	−4.42	−0.731	11.61
328	−4.54		

Table 11
Thermodynamic parameters of BR19 adsorption onto PAA–chitosan–FeMn composite.

Temperature/K	Δ*G*/kJ·mol^{-1}	Δ*H*/kJ·mol^{-1}	Δ*S*/J·mol^{-1}·K^{-1}
298	−6.68		
308	−5.92	−29	75.9
318	−5.16		
328	−4.40		

adsorption of methyl orange on PVP-manganese oxide granular particles the breakthrough curve for the same conditions of the column was observed after 700 min [62].

4. Conclusions

In this study, a dual-charged, non-swelling composite based on polyacrylic acid–chitosan functionalized Fe–Mn mixed oxides was successfully developed and demonstrated high adsorption capacities of 94% for CR, 99.7% for RB19, and 96% for MB. The presence of carboxylic and amine functional groups provided abundant active sites for dye binding, while the Fe–Mn oxide core contributed to structural stability and enhanced adsorption performance. Comprehensive characterization including FTIR, XPS, TGA, SEM, TEM, Raman, and AFM confirmed the structural integrity and functional versatility of the composite before and after dye adsorption. Adsorption experiments revealed removal efficiencies nearly 100% for all dyes at 298 K, and regeneration studies demonstrated that the composite retained >90% of its initial adsorption capacity after six cycles. These results highlight the material's excellent adsorption efficiency, aqueous stability, and reusability, confirming its potential as a robust and multifunctional adsorbent for advanced wastewater treatment applications.

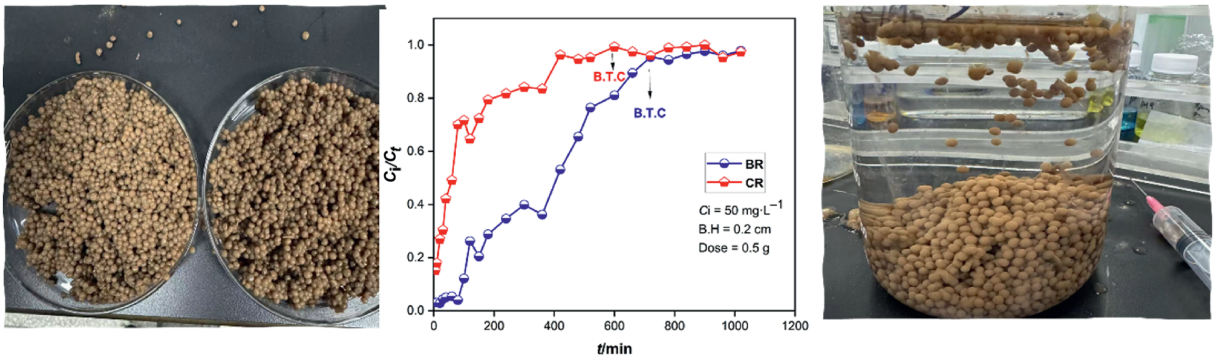

Fig. 15. Breakthrough curves for CR and BR19 onto PAA–chitosan–FeMn composite at initial concentration 50 mg·L^{-1}, at bed hight 0.2 cm, and at 10 ml·min^{-1} rate of flow.

CRediT Authorship Contribution Statement

Afsar Khan: Writing – original draft, Methodology, Investigation, Data curation, Conceptualization. Ran Hong: Writing – review & editing, Data curation, Conceptualization. Saisai Chen: Writing – review & editing, Data curation, Conceptualization. Tingting Liu: Methodology, Investigation. Savaş Kaya: Software. Weihua Chen: Writing – review & editing, Supervision, Project administration. Dayong Xu: Writing – review & editing, Supervision, Project administration, Funding acquisition.

Declaration of Competing Interest

The authors declare the following financial interests/personal relationships which may be considered as potential competing interests: Afsar Khan reports financial support was provided by Anhui Polytechnic University. Afsar Khan reports a relationship with Anhui Polytechnic University that includes: employment.

Acknowledgements

We gratefully acknowledge the funding by the Major Program of Natural Science Foundation for Higher Education Institutions of Anhui Province (2024AH040021) and National College Student Innovation and Entrepreneurship Training Program (202310363071).

References

[1] O.z. Edebali, S. Krupčíková, A. Goellner, B. Vrana, M. Muz, L. Melymuk, Tracking aromatic amines from sources to surface waters, *Environ. Sci. Technol. Lett.* 11 (2024) 397–409.
[2] S. Zhang, Q. Luo, X. Sun, L. Chi, P. Sun, L. Zhang, Facile synthesis copper-modified titania (Cu/TiO_2) nanoparticles for high-efficiency Congo red adsorption, *Chin. J. Chem. Eng.* 81 (2025) 87–94.
[3] M.S. Shukor, K. Aftab, M. Norazlina, H.M.I. Effendi, A.S.R. Sheikh, S.M. Yunus, Isolation of a novel molybdenum-reducing and azo dye decolorizing enterobacter sp. strain Aft-3 from Pakistan, *Chiang Mai Uni. J. Nat. Sci.* 15 (2016) 95–114.
[4] R. Kumaravel, V.K. Shanmugam, Biomimetic and ecological perspective towards decolorization of industrial important Azo Dyes using bacterial cultures–A review, *Sustain. Chem. Environ. (2024) 100130.*
[5] A. Alsbaiee, B.J. Smith, L. Xiao, Y. Ling, D.E. Helbling, W.R. Dichtel, Rapid removal of organic micropollutants from water by a porous β-cyclodextrin polymer, *Nature* 529 (2016) 190–194.
[6] T. Ahmad, Hazardous azo-dyes and aromatic amines from various industrial zones of Punjab province of Pakistan, 19th Global Chemistry, Chromatography & Spectrometry Conference, March 20-21, New York, USA (2019).
[7] H.M. Abd El-Aziz, M.A. Zayed, S.A. Abdel-Gawad, Adsorptive removal of direct red 31 and direct orange 26 azo dyes from aqueous solutions using ficus nano zero valent copper: Linear, non-linear, response surface methodology (RSM), and artificial neural network (ANN) modeling, *Adsorpt. Sci. Technol.* 42 (2024) 02636174241256849.
[8] A. Aslam, F. Batool, S. Noreen, E.A. Abdelrahman, M. Mustaqeem, B.F.A. Albalawi, A. Ditta, Metal oxide-impregnated biochar for Azo dye remediation as revealed through kinetics, thermodynamics, and response surface methodology, *ACS Omega* 9 (2024) 4300–4316.
[9] L. Abramian, H. El-Rassy, Adsorption kinetics and thermodynamics of azo-dye orange II onto highly porous titania aerogel, *Chem. Eng. J.* 150 (2009) 403–410.
[10] A. Khan, A. Naeem, T. Mahmood, B. Ahmad, Z. Ahmad, M. Farooq, T. Saeed, Mechanistic study on methyl orange and congo red adsorption onto polyvinyl pyrrolidone modified magnesium oxide, *Int. J. Environ. Sci. Technol. (2022) 1–14.*
[11] Q. Lu, L. Di, Y. Zhou, Y. Zhou, Efficient removal of bisphenol A from water using a novel organic–inorganic hybrid heterojunction, *Sep. Purif. Technol.* 353 (2025) 128099.
[12] H. Yang, H. Zhang, J. Lu, Y. Cui, Y. Wang, X. Wang, J. Xue, H. Cao, Advanced magnetic adsorbents for enhanced phosphorus and fluoride removal from wastewater: mechanistic insights and applications, *Sep. Purif. Technol.* 353 (2025) 128195.
[13] C. Chen, Z. Yan, Z. Ma, D. Ma, S. Xing, W. Li, J. Yang, Q. Han, Magnetic Fe_3O_4 nanoparticles supported on carbonized corncob as heterogeneous fenton catalyst for efficient degradation of methyl orange, *Chin. J. Chem. Eng.* 77 (2025) 144–155.
[14] Y. Tang, Y. Li, Y. Zhang, C. Mu, J. Zhou, W. Zhang, B. Shi, Nonswelling silica–poly (acrylic acid) composite for efficient and simultaneous removal of cationic dye, heavy metal, and surfactant-stabilized emulsion from wastewater, *Ind. Eng. Chem. Res.* 59 (2020) 3383–3393.
[15] Q.D. Tsauria, P.L. Gareso, D. Tahir, Systematic review of chitosan-based adsorbents for heavy metal and dye remediation, *Integrated Environ. Assess. Manag.* 22 (1) (2026) 26–46.
[16] H. Xia, H. Wang, Y. Zhang, Fabrication and application of magnetic $MgFe_2O_4$-OH@ biochar composites decorated with β-ketoenamine for Pb (II) and Cd (II) adsorption and immobilization from aqueous solution, *Sep. Purif. Technol.* 354 (2025) 129320.
[17] J. Qi, G. Zhang, H. Li, Efficient removal of arsenic from water using a granular adsorbent: Fe–Mn binary oxide impregnated chitosan bead, *Bioresour. Technol.* 193 (2015) 243–249.
[18] C. Lee, W. Yang, R.G. Parr, Development of the Colle-Salvetti correlation-energy formula into a functional of the electron density, *Phys. Rev. B* 37 (1988) 785.
[19] A.D. Becke, Density-functional thermochemistry. III. The role of exact exchange, *J. Chem. Phys.* 98 (1993) 5648–5652.
[20] P.J. Hay, W.R. Wadt, Ab initio effective core potentials for molecular calculations. Potentials for the transition metal atoms Sc to Hg, *J. Chem. Phys.* 82 (1985) 270–283.
[21] I.S. Ufimtsev, T.J. Martinez, Quantum chemistry on graphical processing units. 3. Analytical energy gradients, geometry optimization, and first principles molecular dynamics, *J. Chem. Theor. Comput.* 5 (2009) 2619–2628.
[22] A.V. Titov, I.S. Ufimtsev, N. Luehr, T.J. Martinez, Generating efficient quantum chemistry codes for novel architectures, *J. Chem. Theor. Comput.* 9 (2013) 213–221.
[23] J. Kästner, J.M. Carr, T.W. Keal, W. Thiel, A. Wander, P. Sherwood, DL-FIND: an open-source geometry optimizer for atomistic simulations, *J. Phys. Chem.* 113 (2009) 11856–11865.
[24] T. Goumans, C.R.A. Catlow, W.A. Brown, J. Kästner, P. Sherwood, An embedded cluster study of the formation of water on interstellar dust grains, *Phys. Chem. Chem. Phys.* 11 (2009) 5431–5436.
[25] L.-P. Wang, C. Song, Geometry optimization made simple with translation and rotation coordinates, *J. Chem. Phys.* 144 (2016) 214108.
[26] S. Grimme, J. Antony, S. Ehrlich, H. Krieg, A consistent and accurate ab initio parametrization of density functional dispersion correction (DFT-D) for the 94 elements H-Pu, *J. Chem. Phys.* 132 (2010) 154104.
[27] N. Islam, S. Kaya, Conceptual Density Functional Theory and Its Application in the Chemical Domain, CRC press, (2018).
[28] S. Kaya, C. Kaya, N. Islam, Maximum hardness and minimum polarizability principles through lattice energies of ionic compounds, *Phys. B Condens. Matter* 485 (2016) 60–66.
[29] T. Koopmans, Über die Zuordnung von Wellenfunktionen und Eigenwerten zu den einzelnen Elektronen eines Atoms, *Physica* 1 (1934) 104–113.
[30] A. Wang, B. Li, Y. Wang, X. Sun, Z. Huang, S. Bian, K. Fan, H. Shang, Adsorption behavior of Congo red on a carbon material based on humic acid, *New J. Chem.* 46 (2022) 498–510.
[31] R.-L. Tseng, S.-K. Tseng, F.-C. Wu, Preparation of high surface area carbons from corncob with KOH etching plus CO_2 gasification for the adsorption of dyes and phenols from water, *Colloids Surf. A Physicochem. Eng. Asp.* 279 (2006) 69–78.
[32] L. Chen, D. Zhao, S. Chen, X. Wang, C. Chen, One-step fabrication of amino functionalized magnetic graphene oxide composite for uranium (VI) removal, *J. Colloid Interface Sci.* 472 (2016) 99–107.
[33] J.M. Rosenholm, R.M. Korpi, E. Lammentausta, S. Lehtonen, P. Lehenkari, R. Niemi, W. Xiao, J. Zhang, D. Lindberg, H. Gu, Novel, fast-processed crystalline and amorphous manganese oxide nanoparticles for stem cell labeling, *Inorg. Chem. Front.* 2 (2015) 640–648.
[34] A. Khan, S. Xiao, Y. Xie, S. Kaya, S. Zareen, N. Muhammad, K. Parveen, D. Xu, Rb-promoted Fe/CeO_2 nanocatalyst for aniline conversion into azoxybenzene, DFT calculations and mechanism, *New J. Chem.* 49 (2025) 921–934.
[35] Y. Wang, L. He, G. Dang, H. Li, X. Li, Polypyrrole-functionalized magnetic Bi_2MoO_6 nanocomposites as a fast, efficient and reusable adsorbent for removal of ketoprofen and indomethacin from aqueous solution, *J. Colloid Interface Sci.* 592 (2021) 51–65.
[36] Z. Lan, Y. Lin, C. Yang, Lanthanum-iron incorporated chitosan beads for adsorption of phosphate and cadmium from aqueous solutions, *Chem. Eng. J.* 448 (2022) 137519.
[37] A. Gupta, V.S. Chauhan, N. Sankararamakrishnan, Preparation and evaluation of iron–chitosan composites for removal of As (III) and As (V) from arsenic contaminated real life groundwater, *Water Res.* 43 (2009) 3862–3870.
[38] Y. Haldorai, J.-J. Shim, Multifunctional chitosan-copper oxide hybrid material: photocatalytic and antibacterial activities, *Int. J. Photoenergy* 2013 (2013) 245646.
[39] V. Selen, Ö. Güler, Modeling of Congo red adsorption onto multi-walled carbon nanotubes using response surface methodology: kinetic, isotherm and thermodynamic studies, *Arabian J. Sci. Eng.* 46 (2021) 6579–6592.
[40] N.B. Milosavljević, M.Đ. Ristić, A.A. Perić-Grujić, J.M. Filipović, S.B. Štrbac, Z.L. Rakočević, M.T.K. Krušić, Removal of Cu^{2+} ions using hydrogels of chitosan, itaconic and methacrylic acid: FTIR, SEM/EDX, AFM, kinetic and equilibrium study, *Colloids Surf. A Physicochem. Eng. Asp.* 388 (2011) 59–69.
[41] S. Kaya, C. Kaya, A new equation for calculation of chemical hardness of groups and molecules, *Mol. Phys.* 113 (2015) 1311–1319.

[42] S. Kaya, A. Robles-Navarro, E. Mejía, T. Gómez, C. Cardenas, On the prediction of lattice energy with the fukui potential: some supports on hardness maximization in inorganic solids, *J. Phys. Chem.* 126 (2022) 4507–4516.
[43] M.H. Al-Omari, A. Abu-Rayyan, A.H. Ragab, M.A. Taher, E.-S.M. El-Sayed, A. Elfiky, A. Taha, M.F. Mubarak, Optimized Congo red dye adsorption using ZnCuCr-Based MOF for sustainable wastewater treatment, *Langmuir* 41 (2025) 5947–5961.
[44] M. Özacar, İ.A. Şengil, A kinetic study of metal complex dye sorption onto pine sawdust, *Process Biochem.* 40 (2005) 565–572.
[45] T. Venkatesha, R. Viswanatha, Y.A. Nayaka, B. Chethana, Kinetics and thermodynamics of reactive and vat dyes adsorption on MgO nanoparticles, *Chem. Eng. J.* 198 (2012) 1–10.
[46] T. Mahmood, A. Khan, A. Naeem, M. Hamayun, M. Muska, M. Farooq, F. Hussain, Adsorption of Ni (II) ions from aqueous solution onto a fungus Pleurotus ostreatus, *Desalination Water Treat.* 57 (2016) 7209–7218.
[47] F. Hassan, Y. Shao, B. Mu, Y. Yang, Sorption behavior of artificial keratin fibers from feathers with anionically charged azo and anthraquinone dyes for potential industrial applications, *Int. J. Biol. Macromol.* 284 (2025) 137923.
[48] A. Bukhari, I. Ijaz, H. Zain, E. Gilani, A. Nazir, A. Bukhari, S. Raza, S. Hussain, S. S. Alarfaji, Y. Naseer, Removal of eosin dye from simulated media onto lemon peel-based low cost biosorbent, *Arab. J. Chem.* 15 (2022) 103873.
[49] X.N. Xu, Y.L. Wen, Y.X. Zhao, B. Wang, M.H. Fan, Z.J. Chen, S.Y. Guo, W. Huang, High-efficient removal of dye across a wide pH range over alkali lignin-based adsorbent: batch experiments and DFT mechanistic analysis, *Sep. Purif. Technol. 363 (2025) 132322.*
[50] H. Gao, J. Jiang, Y. Huang, H. Wang, J. Sun, Z. Jin, J. Wang, J. Zhang, Synthesis of hydrogels for adsorption of anionic and cationic dyes in water: ionic liquid as a crosslinking agent, *SN Appl. Sci.* 4 (2022) 118.
[51] Y.S. Reddy, T.J. Jose, B. Dinesh, R.N. Kumar, P.S. Kumar, K. Kaviyarasu, Equilibrium, kinetic, and thermodynamic study of direct yellow 12 dye adsorption by biomass-derived porous graphitic activated carbon, *Biomass Convers. Biorefinery* 15 (2025) 6817–6833.
[52] A. Khan, M. Arif, Z. Han, Y. Xie, C. Ni, Mechanism and performances of methyl orange and Congo red adsorption by MnO_2–PVP composite, *Water Pract. Technol.* 19 (2024) 1047–1060.
[53] Z. Liu, B. Gao, H. Han, Y. Li, H. Fu, D. Wei, A green cross-linking method for the preparation of renewable three-dimensional graphene sponges for efficient adsorption of Congo red dye, *Chin. J. Chem. Eng.* 66 (2024) 84–93.
[54] W. Xiang, X. Zhang, R. Xiao, Y. Zhang, Three-dimensional porous bimetallic metal–organic framework/gelatin aerogels: a readily recyclable peroxymonosulfate activator for efficient and continuous organic dye removal, *Chin. J. Chem. Eng.* 71 (2024) 193–202.
[55] A.M. Aljeboree, F.H. Abdulrazzak, Z.M. Saleh, H.A. Abbas, A.F. Alkaim, Eco-friendly adsorption of cationic (methylene blue) and anionic (Congo red) dyes from aqueous solutions using sawdust, *Eng. Proc.* 59 (2024) 213.
[56] A. Labena, A.E. Abdelhamid, A.S. Amin, S. Husien, L. Hamid, G. Safwat, A. Diab, A.A. Gobouri, E. Azab, Removal of methylene blue and Congo red using adsorptive membrane impregnated with dried Ulva fasciata and Sargassum dentifolium, *Plants* 10 (2021) 384.
[57] H.C. Firmino, E.P. Nascimento, K.C. Costa, L.C. Arzuza, R.N. Araujo, B.V. Sousa, G.A. Neves, M.A. Morales, R.R. Menezes, High-efficiency adsorption removal of Congo red dye from water using magnetic $NiFe_2O_4$ nanofibers: an efficient adsorbent, *Materials* 18 (2025) 754.
[58] M. Harja, G. Buema, D. Bucur, Recent advances in removal of Congo red dye by adsorption using an industrial waste, *Sci. Rep.* 12 (2022) 6087.
[59] H.N. Hamad, S. Idrus, Recent developments in the application of bio-waste-derived adsorbents for the removal of methylene blue from wastewater: a review, *Polymers* 14 (2022) 783.
[60] R.A. Hakro, M. Mehdi, R.F. Qureshi, R.B. Mahar, M. Khatri, F. Ahmed, Z. Khatri, I.S. Kim, Efficient removal of reactive blue-19 dye by co-electrospun nanofibers, *Mater. Res. Express* 8 (2021) 055502.
[61] C. Liang, Q. Shi, J. Feng, J. Yao, H. Huang, X. Xie, Adsorption behaviors of cationic methylene blue and anionic reactive blue 19 dyes onto nanocarbon adsorbent carbonized from small precursors, *Nanomaterials* 12 (2022) 1814.
[62] A. Khan, A. Naeem, T. Mahmood, N. Muhammad, S. Hussain, Fixed-bed column adsorption of methyl orange by poly (vinyl pyrrolidone)-functionalized manganese oxide, *J. Chem. Technol. Biotechnol.* 97 (2022) 2898–2903.